Post-print:
A. Campione, A. Cipollina, E. Toet, L. Gurreri, I.D.L. Bogle, G. Micale, *Water desalination by capacitive electrodialysis: Experiments and modelling*, Desalination. 473 (2020) 114150. https://doi.org/10.1016/J.DESAL.2019.114150

Water desalination by capacitive electrodialysis: experiments and modelling

Antonino Campione[a], Andrea Cipollina[a,], Erwin Toet[b], Luigi Gurreri[a], I. David L. Bogle[c], Giorgio Micale[a]*

[a] *Dipartimento di Ingegneria, Università degli Studi di Palermo, viale delle Scienze Ed.6, 90128 Palermo, Italy*

[b] *FUJIFILM Manufacturing Europe, Oudenstaart 1, 5000 LJ Tilburg, The Netherlands.*

[c]*Centre for Process Systems Engineering, Department of Chemical Engineering, University College London, Torrington Place, London WC1E 7JE, UK.*

[*]*Corresponding Author (A. Cipollina):* andrea.cipollina@unipa.it

Abstract

Electrodialysis-related technologies keep spreading in multiple fields, among which water desalination still plays a major role. A new technology that has not yet been thoroughly investigated is capacitive electrodialysis (CED), which couples the standard ED with capacitive electrodes. CED has a number of advantages such as removal of toxic products and system simplification. Little mention is made of this technology in the literature and, to the best of our knowledge, no modelling works have ever been presented. In this work, the CED process has been studied through experiments and modelling. A CED model is presented for the first time. With a simple calibration based on macroscopic membrane properties and the characterisation of electrode behaviour, the model is able to simulate the dynamics of simple as well as more complex layouts. An original experimental characterisation of electrodes is presented, showing how the collected data can be implemented into

the model. After a successful validation with experimental data, dynamic simulations of a single pass CED unit have been performed with the aim of assessing the effect of different capacitive electrode properties on process performance. Results show how the impact of these properties is different depending on the number of cell pairs.

Keywords: *Dynamic simulation, desalination, ion exchange membrane, electromembrane process, carbon electrode.*

1. Introduction

Electrodialysis (ED) is an electrochemical process that involves the use of ion exchange membranes that are able to selectively orient the motion of either anions or cations [1,2]. The ED unit, often referred to as a stack, is generally based on a plate and frame arrangement, where cation and anion exchange membranes (AEMs and CEMs) are alternatively arranged in series. Channels for water flow are formed in between membranes by separators (i.e. spacers) giving mechanical stability to the channels and promoting mixing [2]. In particular, an AEM, a CEM and two adjacent channels form the repetitive unit, referred as the cell pair (Figure 1). Finally, the device is closed with two end plates.

Upon application of an electric potential, anions and cations start to move in opposite directions. As a result of the alternating presence of CEMs and AEMs, cations will be able to flow through the former, while they will be almost totally blocked by anionic membranes. Conversely, anions will preferentially pass through AEMs. Therefore, ions (and thus salt) can be removed from one channel (referred as the diluate), while being accumulated in the adjacent one (i.e. the concentrate) producing the desalted product as well as a concentrate by-product. In a typical ED stack, current flow is ensured by the presence of faradaic electrodes that are mounted onto the endplates and are connected to a power supply. Therefore, the two end channels (the ones created in between the endplate and the last membrane on each side) are devoted to the circulation of an electrode rinse solution allowing the charge transfer by redox reactions that convert the electronic flux in the external circuit into the ion flux inside the stack. Usually, NaCl or Na_2SO_4 [3,4] are selected as electrolytes.

Capacitive electrodes represent a promising alternative to conventional electrode systems and have been recently proposed in applications for ED and reverse ED [5–7]. Porous capacitive electrodes act as a means of current transport by physico-chemical mechanisms of adsorption and desorption of ions (thus ejecting/capturing electrons) instead promoting electrochemical reactions (Figure 1). There are a number of advantages associated with the use of capacitive electrodes such as the absence of unstable or toxic products (i.e. Cl_2, O_2 and acids or bases, depending on the electrode solution adopted) and the reduction of the electrodic potential drop. In addition, system complexity is reduced due to the absence of the hydraulic circuit that in standard ED is used to recirculate the electrode rinse solution [5,7]. On the other hand, capacitive electrodes suffer from saturation of the carbon layer due to charge accumulation, so that the electrical polarity (as well as concentrate and diluate compartments) needs to be periodically switched in order to operate the desalination process for a long time. However, this drawback is compensated by the fact that ED plants usually operates in ED reversal mode, where a periodical polarity switch is already adopted to address membrane fouling issues. Therefore, such systems are already suitable for the use of capacitive electrodes.

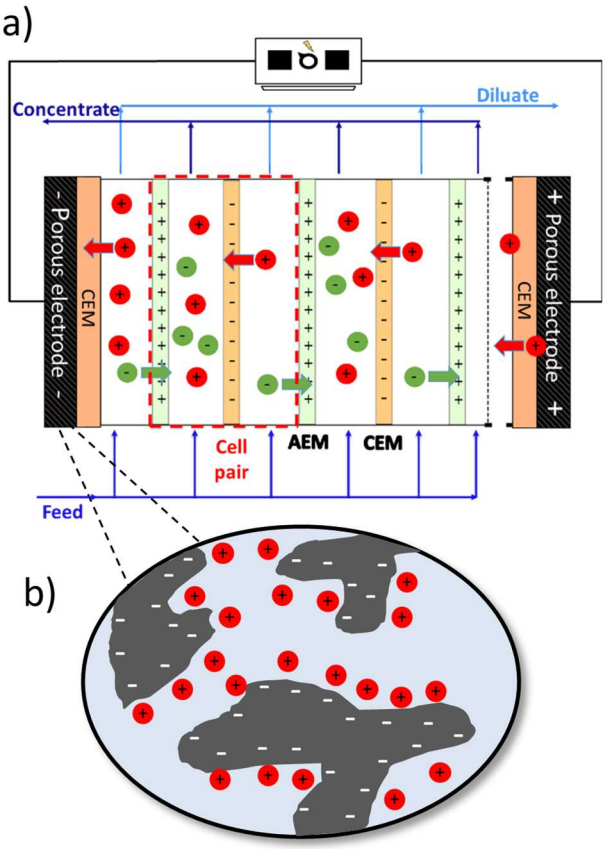

Figure 1. a) Schematic representation of the electrodialysis process with capacitive electrodes (CED), b) detail on the porous structure of the capacitive electrode.

Although a lot of complex phenomena can be involved [8,9], in principle a capacitive electrode is able to store charges in the form of ions through formation of the electric double layer (EDL) upon electrical polarisation [8,10]. As the EDL is formed on the pores' surface, the higher the specific area, the higher the amount of ions that can be stored or released. Therefore, it is imperative to use materials with high surface area in order to avoid too frequent polarity switches. Good conductivity is also desirable, in order to limit the Ohmic losses at the electrodes. For this reason, capacitive electrodes are mainly made from carbon materials [8], although alternatives such as conductive polymers have been also investigated [11]. Among the carbon materials, different authors have reported the use of graphene with various structures such as aerogels [12] multi-layer nanoribbons [13,14], nanotubes [12,15–18] and carbon onions [18,19]. In particular, Portet et al. [18] showed how carbon onions are specifically suitable for energy storage applications, due to their ability to rapidly deliver charges. Another good material is carbon black, which is able to provide a high surface area (> 1500 m^2/g)

through agglomeration of nanoparticles [8,20]. However, the most common electrodes are usually made from activated carbons, characterised by randomly oriented and highly cross-linked graphene layers [21–28]. Activated carbons are particularly attractive as they combine high surface area with low production costs, as they can be produced by natural precursors such as fruit stones [28], leaves [21] and pitch [29].

The ability of capacitive electrodes for storing and delivering ionic charges make them suitable for two fields: conversion and storage of energy, and desalination. In the first one, supercapacitors represent by far the most common application [30,31], although there are some other processes such as Reverse electrodialysis (RED) with capacitive electrodes [7] or with capacitive flow electrodes [32], capacitive cell with CO_2 solutions [33], capacitive double-layer expansion [34] and other CAPMIX technologies [8]. Among the desalination technologies, capacitive electrodes are mostly acknowledged for the capacitive deionisation (CDI) process [35–39]. An interesting development of CDI technology is the single module flow-electrode capacitive deionization (FCDI) [40], which allows the CDI to become a continuous process through the recirculation of an activated carbon suspension. While FCDI has the advantage to be a continuous process, compared to CED it requires a hydraulic electrode circuit. Recently, an FCDI process model was also presented [41].

Although carbon electrodes have been thoroughly studied and applied to many processes and CED is an already commercialised technology [42], to the best of our knowledge the process has not been widely studied in the literature [5,6]. In addition, no CED modelling works have been published yet. In this work, the CED process has been thoroughly studied by means of modelling and experiments. A set of galvanostatic experiments on a lab scale CED stack has been performed with the aim of testing the process desalination capability and characterising a set of capacitive electrodes. In addition, a CED process model is presented. The modelling tool has been implemented by a hierarchical approach that simulates the main dynamic phenomena involved in the CED process and ensures high flexibility in simulating different scales and layouts, ranging from the simple single pass

lab-unit up to complex multistage industrial installations. After a model validation by means of the aforementioned experimental data, simulations have been performed in order to present the predictive capability of the modelling tool and analyse the process performance under a variety of operating conditions.

2. Modelling state of the art

Despite the lack of published CED models, there are a lot of modelling works either on ED [43–56] or on capacitive electrodes applied to other processes [9,57–63].

Many approaches can be adopted to build an ED model, ranging from the simplistic to the more rigorous ones. [2]. Among all the possible approaches, semi-empirical models represent a good balance, as an extensive description of non-ideal phenomena is provided requiring only easily measurable quantities as input parameters (e.g. macroscopic membrane properties). This method has already been presented for both RED [64–66], and ED [49,67–70].

Capacitive electrodes have been extensively modelled at different scales within the context of different applications. In the most basic approach, the electrode is represented by a simple electrical circuit composed by a capacitor and a resistor (*RC circuit model*) [57,58]. Although this approach does not take into account the physical structure of the carbon material, all the electrode characteristics are condensed into the values of the two electrical elements that are relatively easy to measure. Therefore, this simple yet effective approach is particularly useful for process models as it requires little yet easily accessible information.

A more detailed approach to the problem is represented by the *transmission line model* [10,58,71,72]**.** In this case, the porous electrode structure is approximated through a complex circuit with electrical elements (i.e. resistor, capacitors and impedances) arranged in series and parallel. Different degrees of complexity can be found based on the assumed porous structures, ranging from simple RC

transmission lines [71,72] up to a complex arrangement of hierarchical impedances where a bimodal porous structure is required [10]. This type of model can be calibrated on a specific capacitive electrode by quantifying a set of fitting parameters in the form of electrical elements by means of electrical impedance spectroscopy measurements [10].

A completely different approach is based on the theoretical description of the EDL. Traditionally, models belonging to this category are based on the Gouy-Chapman-Stern theory [9,60,61]. Alternatively, the Donnan and modified Donnan models provide a more comprehensive description, involving the dynamics of EDL formation and accounting for overlapping EDLs typical of small pores [59,63,73,74]. The latter class of models can also be extended to account for non-electrostatic ion adsorption [59] and faradic reactions [63]. Theoretical models for capacitive electrodes can predict electric potential distributions inside the pores. However, complex parameters, such as the capacitance of micropores [59], need to be estimated.

In the CED model developed in this work, an existing semi-empirical hierarchical ED model [70] was properly modified and extended to account for the presence of capacitive electrodes which were modelled by means of a distributed RC circuit.

3. Model

A dynamic CED hierarchical model was developed. The starting point for the current formulation is a pre-existing steady-state ED one-dimensional process simulator [70] that was adapted for the purpose of accounting for the peculiarities of the new process. Consequently, existing hierarchies were modified to take into account the intrinsic dynamic behaviour, allowing for all the variables to be also function of time (Figure 2).

Starting from the lowest scale, the model simulates mass transport and electrical behaviour of the cell pair (i.e. the ED repeating unit) and the capacitive electrodes. These two elements are coupled in the

second level where the whole stack is modelled (Figure 2 c). Finally, the stack model is implemented in the plant model, i.e. the highest scale that can simulate different process layouts (i.e. single stage, multistage, batch, feed and bleed etc.).

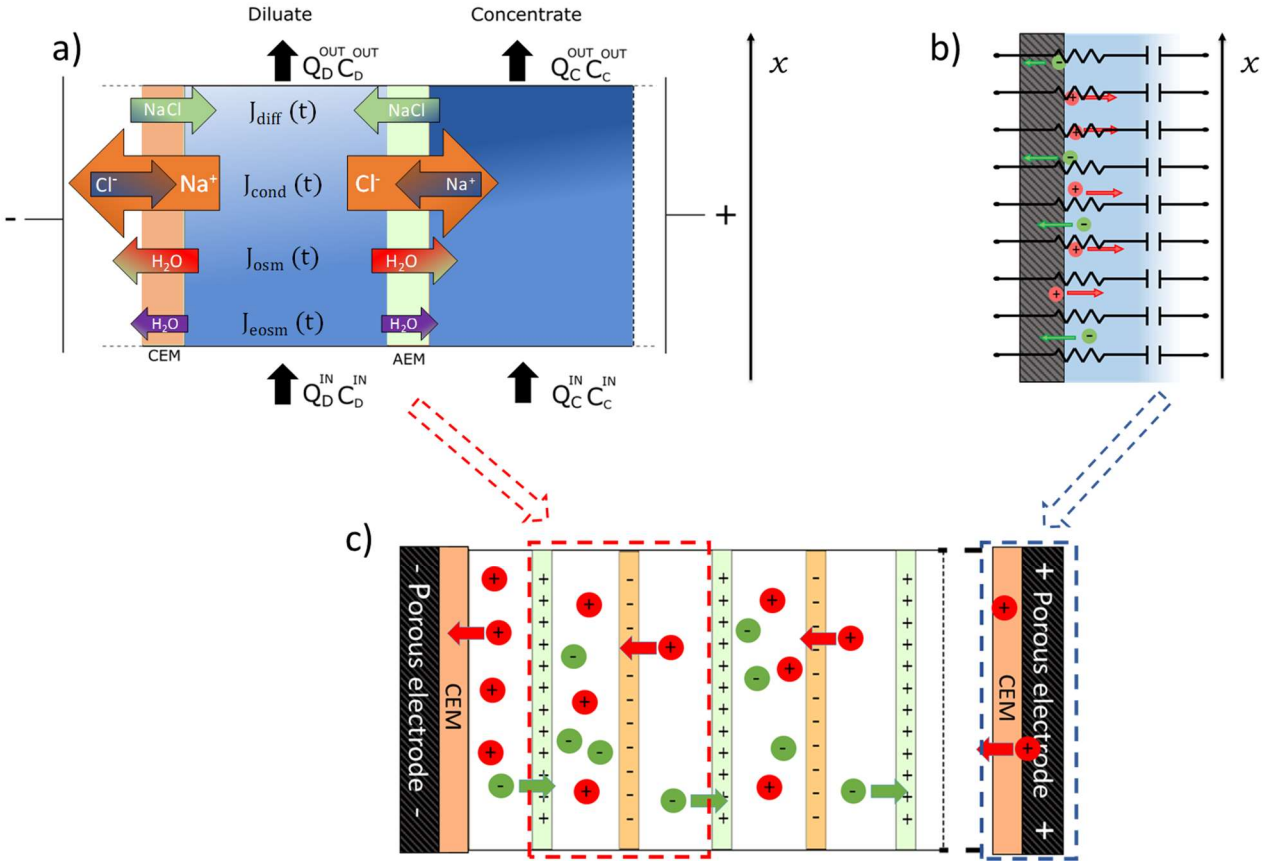

Figure 2. Schematic representation of the model hierarchies. a) Cell pair, b) capacitive electrode, c) stack.

3.1 Capacitive electrodes model

Each capacitive electrode was modelled as a distributed entity divided into a number of discretisation intervals in the direction of the channel length (Figure 2 b). A simple RC circuit was used to model the behaviour of each interval. No contributions for unwanted faradic reactions or non-electrostatic adsorption was considered. Therefore, the time-dependent distributed electrode voltage drop (indicated as V_{el}) can be written as:

$$V_{el}^{j}(x,t) = \frac{\sigma_{el}^{j}(x,t)}{c_{el}^{j}(x,t)} + R_{el}^{j} i(x,t) \tag{1}$$

where σ_{el} is the amount of charge per unit of projected area collected by the capacitor at a given time and position, c_{el} is the electrode capacitance per unit of projected area, R_{el} the electrode areal resistance, $i = \frac{d\sigma_{el}}{dt}$ is the current density and x and t are the space and time coordinates respectively. The superscript j represents the fact that the equation is valid for both of the electrodes in the CED unit. It is worth noting that, considering a spatial distribution, each discretised electrode volume can behave differently from others, thus potentially having different values of charge, capacitance, resistance and, thus, voltage at every x. This assumption has been made in order to account for the fact that in a real unit the electrode can be subjected to a very different concentration and current density along the channel direction, thus potentially making it behave very differently from the inlet to the outlet of the stack. Figure 3 shows the charge spatial distribution of a capacitive electrode as well as the current density spatial variation, highlighting how much these variables can change along the channel length.

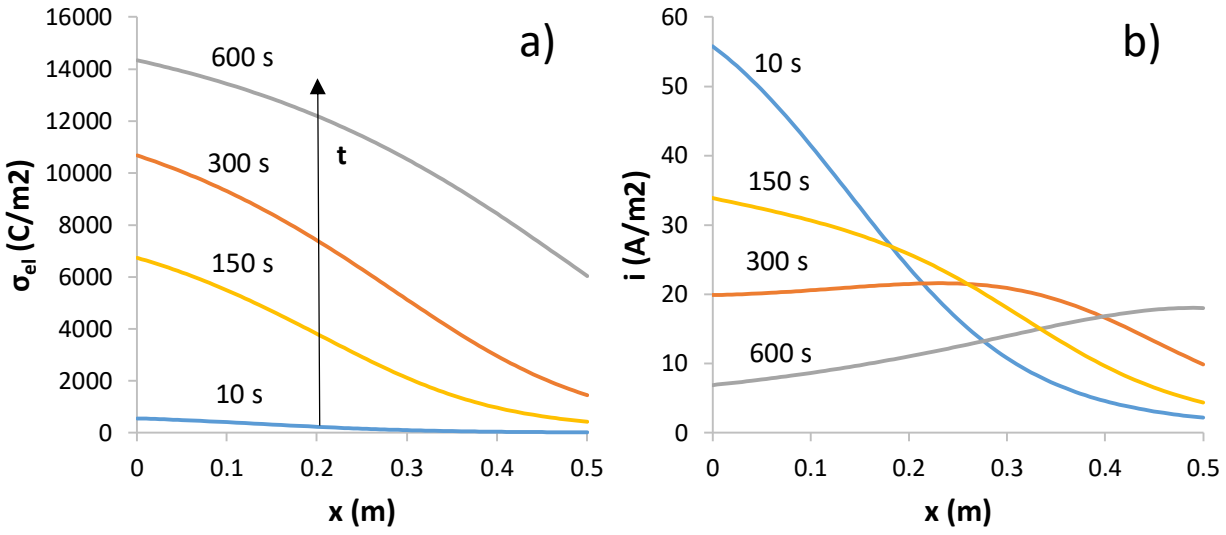

Figure 3. Spatial distribution of a) capacitive electrode charge and of b) current density along the channel length, at different times for the simulation a single pass CED unit 12.5 cm wide and 80 cm long, equipped with 270 µm woven spacers and FUJIFILM capacitive electrodes (RC circuit properties taken from experimental results). Inlet concentration of 2 g/l, linear velocity of 2 cm/s, and ±2 V of applied voltage with polarity switches every 600 s (10 min).

In this work, the value of c_{el} was experimentally determined as a function of the solution concentration by means of galvanostatic methods (see section 4).

3.2 Cell pair model

The cell pair model has also distributed parameters and includes salt and water mass balances and transport equations (Figure 2 a), electrical equations and correlations for the estimation of thermodynamic properties of salt solutions and membranes [70]. Table 1 summarises the main equations implemented in the model. For the meaning of all quantities, refer to the list of symbols. For the sake of clarity, a complete description of the cell pair model can be found in the supplementary material.

Table 1. List of the main equations for mass transport in the cell pair model.

Described phenomenon	Equation	
Salt mass balance	$b\,\delta_{SOL}\frac{\partial C_{SOL}(x,t)}{\partial t}+\frac{\partial Q_{SOL}(x,t)C_{SOL}(x,t)}{\partial x}=\pm b\,J_{tot}(x,t)$	(2)
Overall mass balance	$\frac{d\,Q_{SOL}(x,t)}{dx}=\pm\,b\,q_w(x,t)$	(3)
Conductive salt flux	$J_{cond}(x,t)=\,[t_{CEM}^{counter}-(1-\,t_{AEM}^{counter})]\,\frac{i\,(x,t)}{F}$	(4)
Diffusive salt flux	$J_{diff}^{IEM}(x,t)=-\frac{D^{IEM}}{\delta^{IEM}}({C_C}^{int,IEM}(x,t)-{C_D}^{int,IEM}(x,t))$	(5)
Overall salt flux	$J_{tot}(x,t)=\,J_{cond}(x,t)+\,J_{diff}^{AEM}(x,t)+\,J_{diff}^{CEM}(x,t)$	(6)
Osmotic water flux	$q_{osm}^{IEM}(x,t)=L_p^{IEM}\left(\pi_C^{IEM}(x,t)-\pi_D^{IEM}(x,t)\right)$	(7)
Electroosmotic water flux	$q_{eosm}(x,t)=\,\frac{w\,J_{tot}(x,t)M_w}{\rho_w}$	(8)
Overall water flux	$q_w(x,t)=\,q_{osm}^{AEM}(x,t)+q_{osm}^{CEM}(x,t)+q_{eosm}(x,t)$	(9)

In contrast to the original steady-state model, most of the variables are now intrinsically functions of time (t) as well as space (x) and salt material balances (eq.(2)) have the time derivative term.

The cell pair electrical terms are also computed at this scale. Interestingly, due to the discretisation of the capacitive electrodes (whose model is coupled with the cell pair model at the stack level), it is not possible to define a single voltage drop over a cell pair (V_{cp}) independent from the spatial coordinate. In fact, only in the stack, where current collectors impose an equipotential surface, is it possible to define a unique value of the voltage (for more details, see section 3.3). Therefore, V_{cp} is different for each single branch of the cell pair equivalent electrical circuit, thus becoming a function of x. According to the cell pair equivalent circuit (depicted between the brackets in Figure 4):

$$V_{cp}(x,t) = \eta\,(x,t) + R_{tot}(x,t)i(x,t) \tag{10}$$

where η is the non-Ohmic voltage drop associated to the back electromotive force where concentration polarisation is also taken into account making use of computationally determined Sherwood numbers [70,75–77] and R_{tot} is the total areal Ohmic resistance of cell pair which can be calculated as the sum of membrane and solution compartment resistances [70].

3.3 Stack model

The stack model simulates a series of cell pairs between two capacitive electrodes which are positively or negatively polarised. Within the stack, it is possible to compute power consumption, performance parameters (e.g. current efficiency) and overall quantities such as the applied voltage [70]. At a given time, performance parameters are defined as in the classical ED process, while the external applied voltage (V_{tot}) can be calculated by summing up the voltage drop of all cell pairs and of the two electrodes at any position (according to the system equivalent circuit shown in Figure 4):

$$V_{tot}\,(t) = \left(\sum_{i=1}^{Ncp} V_{cp_i}(x,t)\right) + V_{el}^{1}(x,t) + V_{el}^{2}(x,t) \tag{11}$$

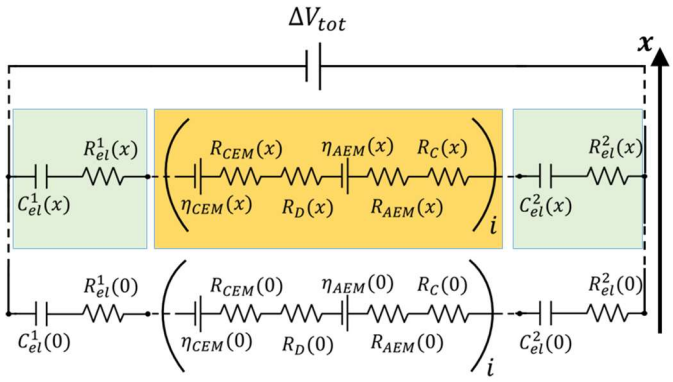

Figure 4. Scheme of the distributed equivalent electrical circuit representative of the stack model, including the cell pair circuit (in brackets) in series with the RC elements of the capacitive electrodes. For the sake of brevity, only the branches that describe the position x = 0 (channel inlet) as well as one for a generic x position have been explicitly represented.

Despite the fact that the voltage of each element (i.e. cell pairs and the two electrodes) can be different at each x position, the total voltage is a single parameter. This represents the value that can be externally measured at the current collectors.

3.4 Plant model

The plant model represents the highest hierarchy of simulation where a number of stack models can be variously arranged together with other auxiliary units. In a previous paper [70] multistage and batch configurations for standard ED have been assessed highlighting the operating advantages of some possible arrangements. However, more complex layouts can also be simulated, including the presence of recycle streams, typical of feed and bleed configurations.

4. Experimental

A 10×10 cm^2 bench-scale CED unit (*Deukum GmbH, Germany*), equipped with carbon capacitive electrodes with graphite current collectors (*FUJIFILM Manufacturing Europe B.V., The Netherlands*), operating in a single pass co-flow arrangement was tested. The stack was assembled with 10 cell pairs made by Type 10 ion exchange membranes (*FUJIFILM Manufacturing Europe B.V., The Netherlands*) whose main properties are listed in Table 2, and 270 µm woven spacers (*Deukum GmbH, Germany*) [78]. CEM end-membranes have been placed in direct contact with the

electrodes, so that only cations are involved in the formation of EDL at the electrodes. For this reason, during the operation one capacitor will accumulate cations while the other will desorb them. A schematic representation of the stack assembly is provided in Figure 5.

Table 2. Properties of Type 10 FUJIFILM membranes (experimentally measured).

Membrane	Thickness δ (µm)	Permselectivity α*	Water permeability L_p (ml/(bar h m^2))	Resistance R (Ω·cm^2)**
AEM	130	0.969	6.29	1.77
CEM	130	0.975	7.79	1.89

*Permselectivity measured in between 0.05M/0.5M KCl solutions

**Membrane resistance measured with 0.5 M NaCl solution

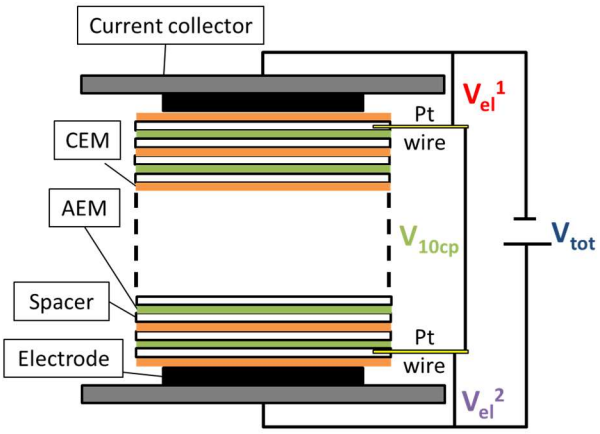

Figure 5. Schematic representation of the CED unit used for the experiments. V_{tot} ,V_{el}^1,V_{el}^2 and V_{10cp} indicates the experimentally measured voltage drops: overall voltage drop (V_{tot}), electrode 1 voltage drop (V_{el}^1), electrode 2 voltage drop (V_{el}^2), cell pairs voltage drop (V_{10cp}).

NaCl solutions at different concentrations (1, 3, 5 and 10 g/l) were pumped with a flowrate of ~ 490 ml/min (3 cm/s) through the stack using DC controlled diaphragm pumps controlled by flow meters (Krohne, Germany). Solution conductivities have been measured and continuously monitored both at the inlet and at the outlet through conductivity meters (LAQUA F-74, HORIBA *Ltd., Japan*)

The experiments were performed under galvanostatic conditions (constant current) by means of a power supply (PPS-11815, Voltcraft*, Germany*). Platinum wires of 0.2 mm diameter (Agar Scientific Ltd., UK) were used to measure the voltage drop over the membrane pile excluding the electrodes (V_{10cp}, as shown in Figure 5) and over the single electrodes (V_{el}^1 and V_{el}^2 from Figure 5). Voltages have been continuously measured and recorded through an acquisition system (M300, *Rigol Technologies Inc., U.S.*).

During a single galvanostatic test, a constant current has been maintained for a chosen time period in order to avoid excessive voltage over the electrodes, and thus the occurrence of water splitting. At the end of the period, a polarity switch inverted the direction of the fixed current (Figure 6 a). The switches were repeated for a number of cycles in order to ensure the achievement of a regular periodic operation.

Figure 6 a shows an example of the electrical voltages measured during a typical experiment. Apart from V_{tot}, the graph depicts V_{el}^1, V_{el}^2 and V_{10cp}. It is worth noting that the voltages are always represented as voltage drops (so that $\sum V_i = V_{tot}$). Therefore, when a positive current (orange line) is applied, V_{el}^1 represents the voltage drop of the electrode that is adsorbing cations (and thus acting as a *passive* charging element), while the negative value of V_{el}^2 is representative of the electrode that is actively discharging and thus providing part of the current. The opposite happens when a negative current is applied.

From the V_{tot} *vs* time curves obtained from the experiments, it was possible to estimate the equivalent capacitance of the electrodes by means of the following equation:

$$\frac{dV_{tot}}{dt} = \frac{i}{c_{el}^{eq}} \tag{12}$$

where $\frac{dV_{tot}}{dt}$ is the slope of the overall voltage *vs* time curve (linear parts of V_{tot} curve as in Figure 6 b), i is the overall current and c_{el}^{eq} is the equivalent areal electrode capacitance, accounting for both

capacitive electrodes. If the charging (or discharging) voltage curve of the two electrodes is almost equivalent, it can be assumed that their behaviour is the same. Consequently, the capacitance of a single electrode can be taken as twice as the value estimated from eq.(12). In the case of highly asymmetric behaviour (i.e. when two completely different electrodes are used at each side of the CED unit), the capacitance of the each electrode can be also deduced directly from the slope of each V_{el}^{j} voltage curve.

At a given feed concentration (which was assumed as the concentration inside the stack channels due to the high flowrate), the capacitance has been averaged over each value measured from positive and negative voltage curves. In addition, each experiment was repeated 2 to 3 times.

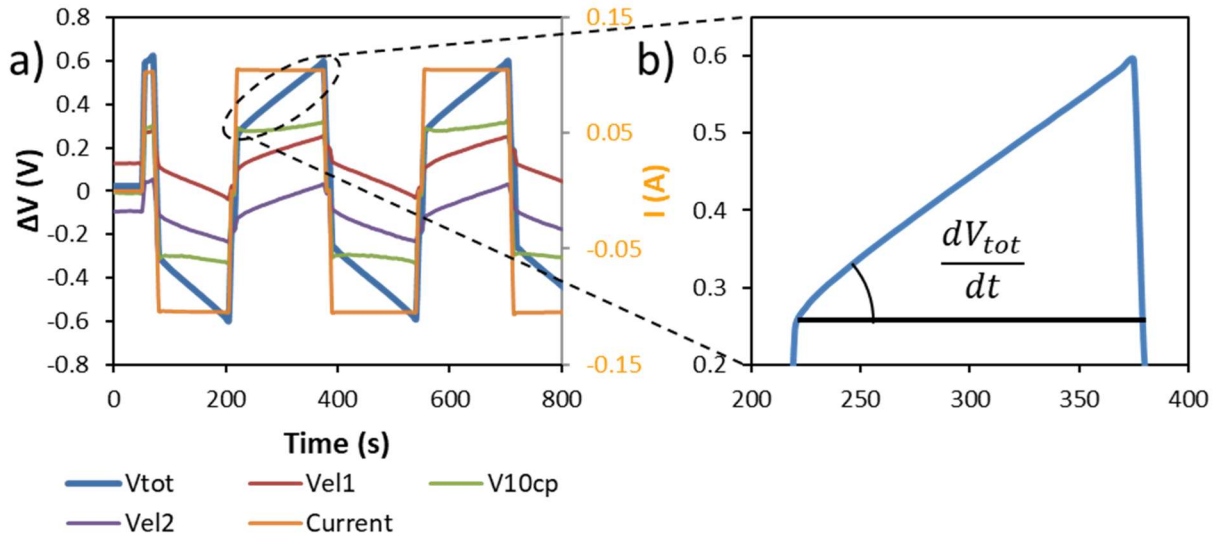

Figure 6. a) Representation of a typical experimental voltage vs time curve showing the overall voltage drop (V_{tot}), electrode 1 voltage drop (V_{el}^{1}), cell pairs voltage drop (V_{10cp}), electrode 2 voltage drop (V_{el}^{2}) and the applied current. b) Detail of a linear part of V_{tot} vs time curve used for the estimation of electrode capacitance. The graphs refer to a 1 g/l feed concentration and ±0.1 A, where positive or negative sign of the current indicates the two different polarities.

5. Results and discussion

In the first part of this section, the results from the experimental capacitance measurements are shown. Then, predictions of the CED process simulations, performed with the experimentally determined values of electrode capacitance, are compared with the experimental data of the CED unit for

validation purposes. Finally, simulation results aimed at assessing the influence of capacitive electrode parameters and number of cell pairs on the process performance are presented and discussed.

5.1 Bench-scale CED stack

5.1.1 In-situ experimental characterization of the capacitive electrodes

Figure 7 shows the specific capacitance per cm^2 of projected area estimated from the overall voltage versus time curves (c_{el}^{eq}) as a function of solution concentration. Error bars have been determined from the standard deviation of the outcomes of each repeated experiment. The slightly increasing trend of the capacitance can be explained by the formation of an electric double layer at the nanoscopic scale which is influenced by the amount of ions in the solution, as traditionally formulated by the Gouy-Chapman model of the diffuse EDL [79]. Given the common nature of the two electrodes of this specific unit (see section 4), the capacitance of a single electrode has been taken as twice the value reported in Figure 7 as discussed in section 4.

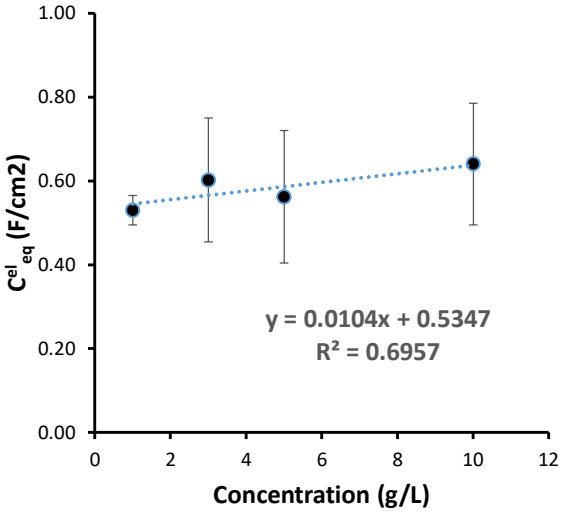

Figure 7. Measured specific overall electrodes capacitance (c_{el}^{eq}) as a function of solution concentration.

5.1.2 Experimental characterization of the CED unit and model validation

The correlation of the capacitance *vs* the concentration obtained from the experimental results has been implemented into the capacitive electrode model of the CED process simulator in order to predict the behaviour of the experimentally characterised electrodes. Therefore, it was possible to assess the model reliability in simulating the operation of the CED unit by comparison with the experimental curves. *gProms Modelbuilde*r (*PSE, UK*) has been used as simulation platform.

Simulations were performed by applying the electrode open circuit voltages (i.e. measured when no current was flowing through the system) as initial condition. Those voltages are associated with the fact that a certain amount of charge is already accumulated at the electrode surface. In addition, the value of the electrode ohmic resistance was calibrated from the instantaneous step voltage response of each electrode when the current is applied (Figure 8 c and Figure 9 c) and ranged from 50 to 100 $\Omega \cdot m^2$, based on solution concentration.

Figure 8 shows simulation results in comparison with the experimental data for the case of 10 g/l feed and ±0.15 A current. As shown, the process is actively desalinating one feed stream while concentrating the other (Figure 8 d). At a given polarity, the cell pair voltage stays constant as the desalination rate is kept constant by the applied current. On the other hand, the absolute value of V_{el}^1 and V_{el}^2 (Figure 8 c) grows in order to maintain the desired current. Interestingly, after the first two cycles the operation is quite stable and able to maintain the same performances for multiple cycles. Therefore, it seems realistic to imagine wider CED stacks (i.e. with larger active area) that can steadily desalinate a feed stream down to the drinking water concentration target.

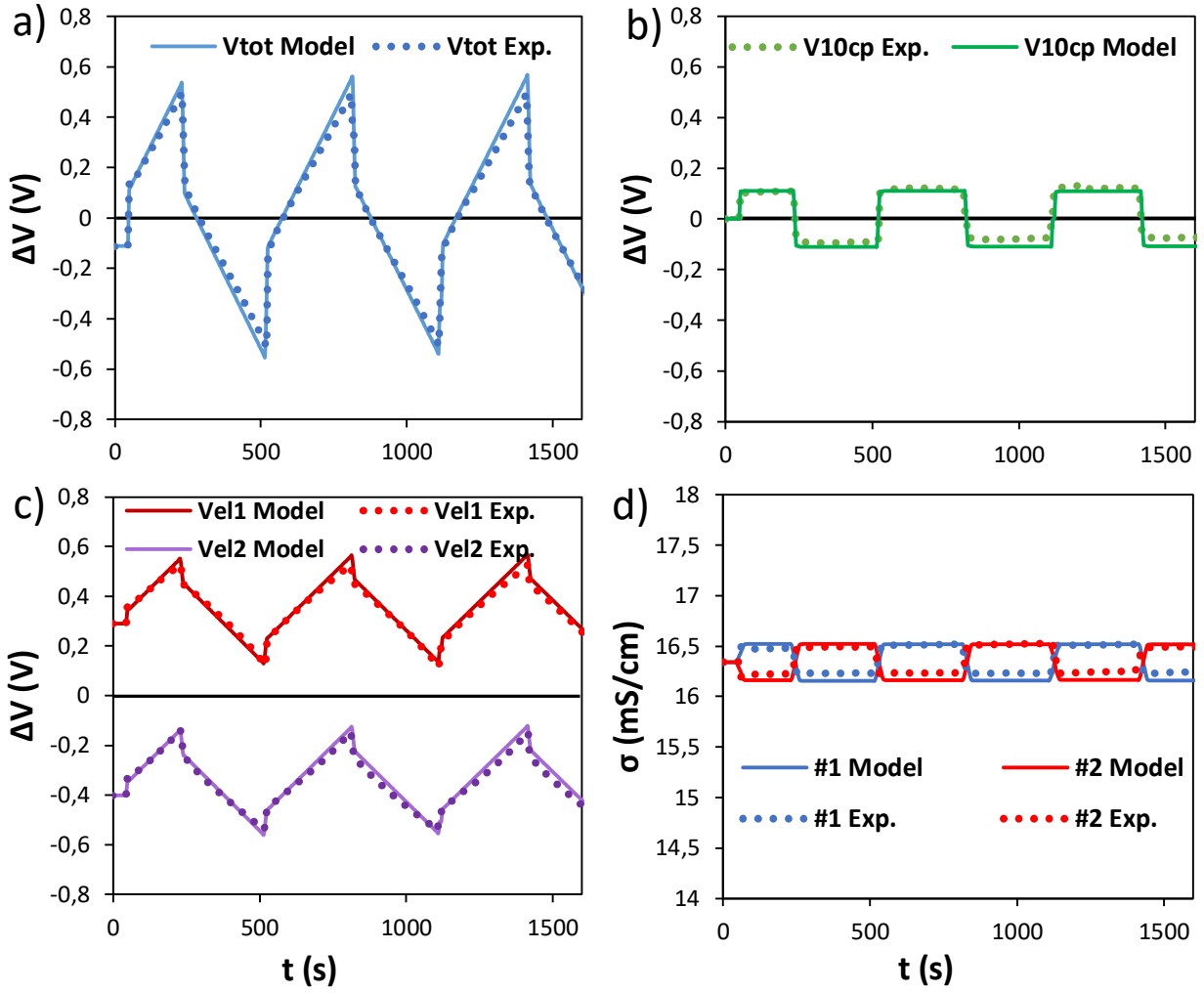

Figure 8. Model predictions compared with experimental data of a bench-scale 10×10 cm² CED stack equipped with 270 µm woven spacers and Type 10 FUJIFILM membranes. Inlet concentration of 10 g/l flowrate of 486 ml/min and applied current of ±0.15 A with polarity switches every ~280 s. a) Overall voltage drop, b) Cell pairs voltage drop, c) Electrodes voltage drop, d) outlet conductivity of the two compartments.

Other operating conditions have been tested through both experiments and simulations. For example, Figure 9 shows the case of 1 g/l of salt concentration and ±0.1 A current. Similarly to the previous case, the desalination capability has also been demonstrated for lower concentration feeds. The main difference is that in this case the cell pair voltage drop (Figure 9 b) is much higher compared to the one in Figure 8 b due to the lower solution conductivity. Consequently, shorter cycles have been

performed in this case, despite the fact that the slope of the total voltage curve (Figure 9 a) is flatter due to the lower applied current.

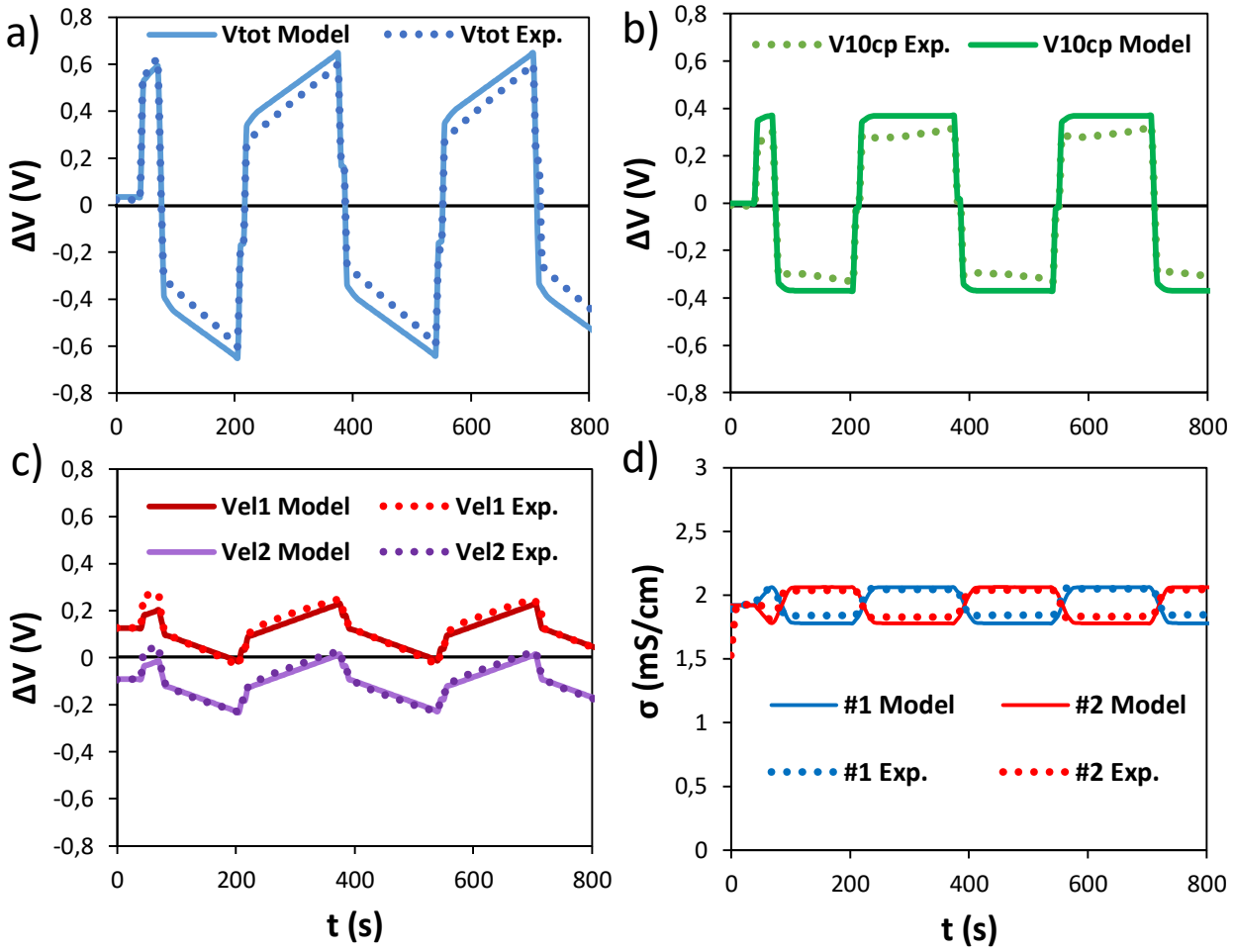

Figure 9. Model predictions compared with experimental data of a 10×10 cm² CED stack equipped with 270 µm woven spacers and Type 10 FUJIFILM membranes. Inlet concentration of 1 g/l, flowrate of 486 ml/min and applied current of ±0.1 A with polarity switches every ~180 s. a) Overall voltage drop, b) average cell pairs voltage drop, c) electrodes voltage drop, d) outlet conductivity of the two compartments.

In general, Figure 8 and Figure 9 demonstrate that the model has a good prediction capability at different operating conditions both for the voltage *vs* time curves, as well as for the outlet conductivities. However, the model shows a slight overestimation of the average cell pair voltage drop (Figure 9 b). This discrepancy can be attributed to the stack assembly. According to the scheme

of Figure 5, the dimensions of the carbon electrodes are limited to the 10×10 cm^2 active area and no external gaskets are used to compensate for the localized increase of thickness that takes place in the central part of the stack. Therefore, when the stack is closed, the electrodes apply a localized pressure on the active area of the membranes that are directly compressed over the spacer netting, reducing the real thickness of the channels and thus the channel Ohmic resistance. For low feed concentrations (as for the 1 g/l case) the resistance is higher and the difference between the real and the nominal value of the resistance increases the differences between the predicted and the measured voltage values.

5.2 Performance prediction of large-scale CED stacks

In real scenarios, salty water feeds need to be desalted down to drinking water salt concentration. In order to apply the CED technology to those cases, larger units must be considered. In this context, the model is a suitable tool to analyse the process in wider and more industrially-relevant conditions.

Following the model validation, a single pass CED operation was simulated for a scaled-up configuration with 12 cell pairs and an active area of 12.5 (width) × 80 (length) cm^2. A resistance of 50 $\Omega \cdot cm^2$ has been attributed to the electrodes (see section 5.1.2). Starting from a reference case, the CED model has been used to assess the effect of the electrode features on the process performance (section 5.3.1 and 5.3.2).

The CED unit had to desalt a 2 g/l NaCl feed solution flowing with a linear velocity of 2 cm/s. This time, potentiostatic operations with a constant voltage of ±2 V have been simulated as this mode of operation is the most common in commercial applications. Multiple polarity switches were performed every 10 minutes (600 s). It is worth noting that the chosen switching time is not too far from the usual switching time of EDR plants (between 15 and 30 minutes). In order to simulate the CEM end membrane scheme, the electrode that is accumulating charge during the first cycle has a zero charge initial condition, while the opposite electrode is assumed to be pre-charged with a Q_{el} of 1 C/cm^2.

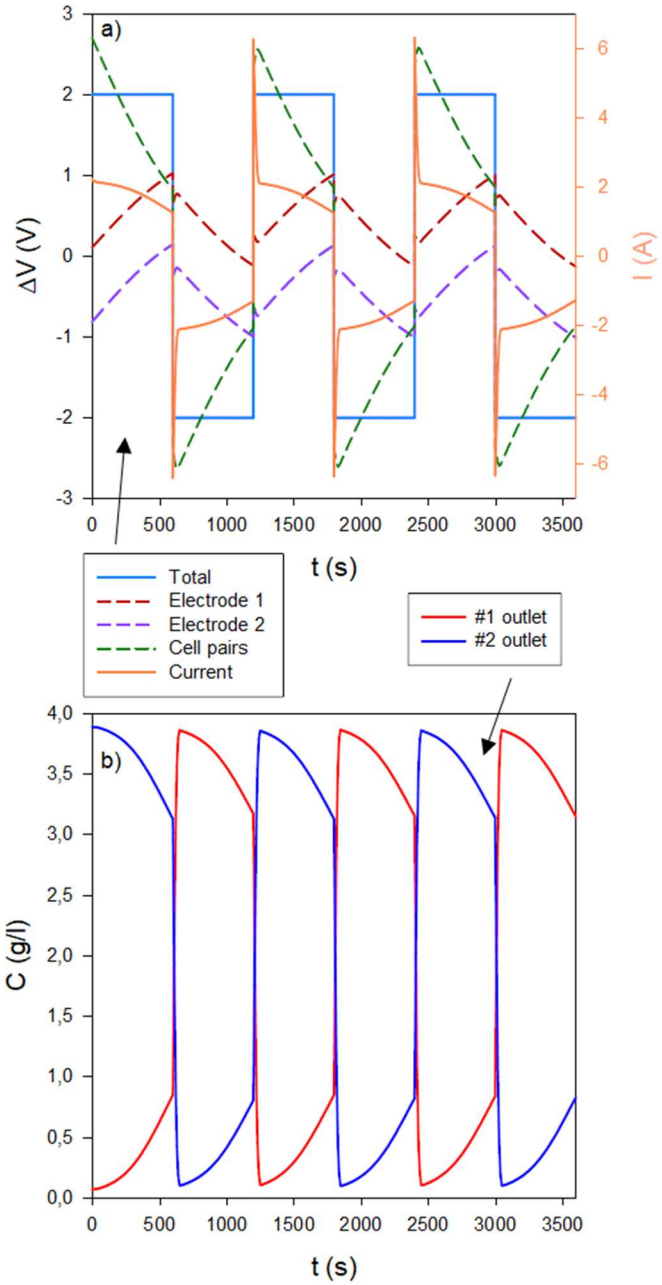

Figure 10. Simulation results of a single pass CED unit 12.5 cm wide and 80 cm long equipped with 270 µm woven spacers and FUJIFILM capacitive electrodes (RC circuit properties taken from experimental results). Inlet concentration of 2 g/l, linear velocity of 2 cm/s, and ±2 V of applied voltage with polarity switches every 600 s (10 min). a) Overall, electrodes and cell pair voltage drop and current vs time, b) outlet concentrations of the two streams vs time.

Simulation results are reported in Figure 10. In particular, Figure 10 a depicts the electrical variables as a function of time. At the beginning of a cycle, electrode 2 (i.e. the pre-charged one that is rejecting cations) is actively providing a voltage in addition to the external applied voltage (of 2V) that is higher than the actual electrode 1 voltage drop. Therefore, a voltage higher than 2 V is really applied to the cell pairs. However, during constant voltage operation, the electrodes' voltage changes, thus causing

a decrease of (the absolute value of) the cell pairs' voltage. Because of this phenomenon, the overall current decreases, negatively affecting the desalination rate during a cycle and thus causing the diluate outlet concentration to increase up to 0.8 g/l at the end of the cycle, as shown in Figure 10 b.

The simulated reference case of CED operation would likely present some critical issues when replicated in a real unit. Firstly, the electrode voltage goes above 1 V in the last part of each cycle, meaning that unwanted faradic reactions (i.e. water splitting) may occur at to a large degree and damage at the electrodes may occur. In addition, the diluate outlet concentration increases well above the freshwater limit (set to 0.5 g/l, but usually taken even lower as a safety precaution). Therefore, with these electrodes shorter switching intervals would be required.

5.2.1 Effect of electrode capacitance on single pass CED

In order to avoid the aforementioned critical issues, maintaining the set switching interval or even extending it, the electrode should have an enhanced capacity. In this way, the electrodes' voltage would grow less through time, causing a slower drop in the overall current. The latter effect would also make an impact on the diluate outlet concentration slowing down its increase. In order to numerically evaluate the improvements, the effect of electrode capacitance on process performance has been assessed via simulations. In particular, the specific capacitance per electrode was increased from ~ 1.2 F/cm^2 for the reference case to 2 and 3.3 F/cm^2. In this sensitivity study, the two latter values of capacitance are taken as constant values (i.e. independent from solution concentration) for the sake of simplicity.

Simulation results are reported in Figure 11. Comparing the reference capacitance with 2 F/cm^2, the slope of the capacitive electrodes' voltage over time is already strongly reduced, thus not reaching the undesired 1 V threshold through the 600 s of constant polarity (Figure 11 a). In addition, desalination performances are also enhanced (Figure 11 b). At 2 F/cm^2, the diluate concentration goes

only slightly over 0.5 g/l, achieving an acceptable result, as the outlet solution produced in the earliest part of the cycle (whose concentration was well below the limit) will be in the end mixed with the more concentrated solution exiting at the end of the cycle. Interestingly, a further increase in the capacitance up to 3.3 F/cm^2 does not provide a significant improvement to the voltage even though it still makes an impact on the outlet concentration.

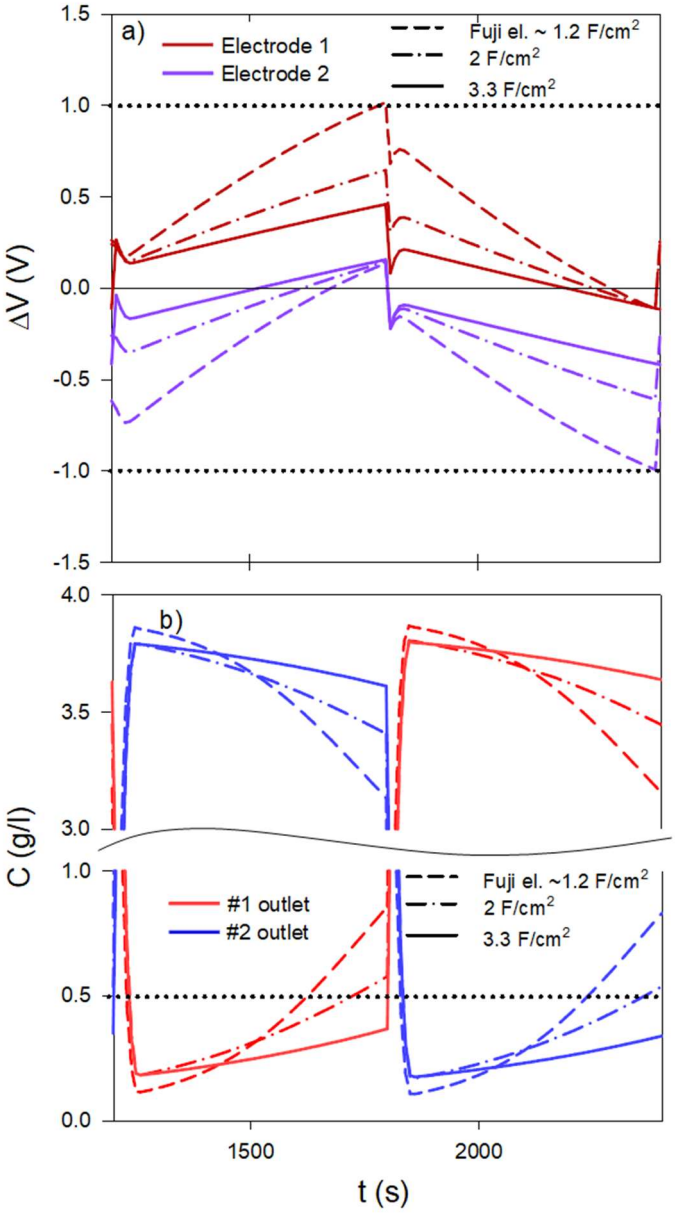

Figure 11. Simulation results for the comparison of different electrode capacitances (~ 1.2, 2 and 3.3 F/cm^2) in a single pass CED unit 12.5 cm wide and 80 cm long equipped with 270 µm woven spacers and FUJIFILM capacitive electrodes (RC circuit properties taken from experimental results). Inlet concentration of 2 g/l, linear velocity of 2 cm/s, and ±2 V of applied voltage with polarity switches every 600 s (10 min). a) Electrodes voltage drop vs time, b) outlet concentrations of the two streams vs time.

5.2.2 Effect of electrode resistance on single pass CED

The specific electrode resistance is another interesting parameter to analyse. The reference value of 50 Ω*cm^2 has been compared with a doubled resistance (100 Ω*cm^2) as well as with a halved one (25 Ω*cm^2), maintaining the reference value of capacitance. Figure 12 shows the results in terms of electrode voltage and outlet concentration *vs* time. The increase in resistance causes a slight increase in the voltage as well as in the diluate concentration (due to a reduction in the stack current density). The reduction of the electrode resistance has the opposite effect. Nevertheless, the influence of the electrode resistance is almost negligible , as it is relatively small compared to the average Ohmic resistance of the 12 cell pairs amounting to ~ 500 Ω*cm^2 . Consequently, a reduction in resistance does not lead to appreciable improvements of the process performance as an increase of capacitance does.

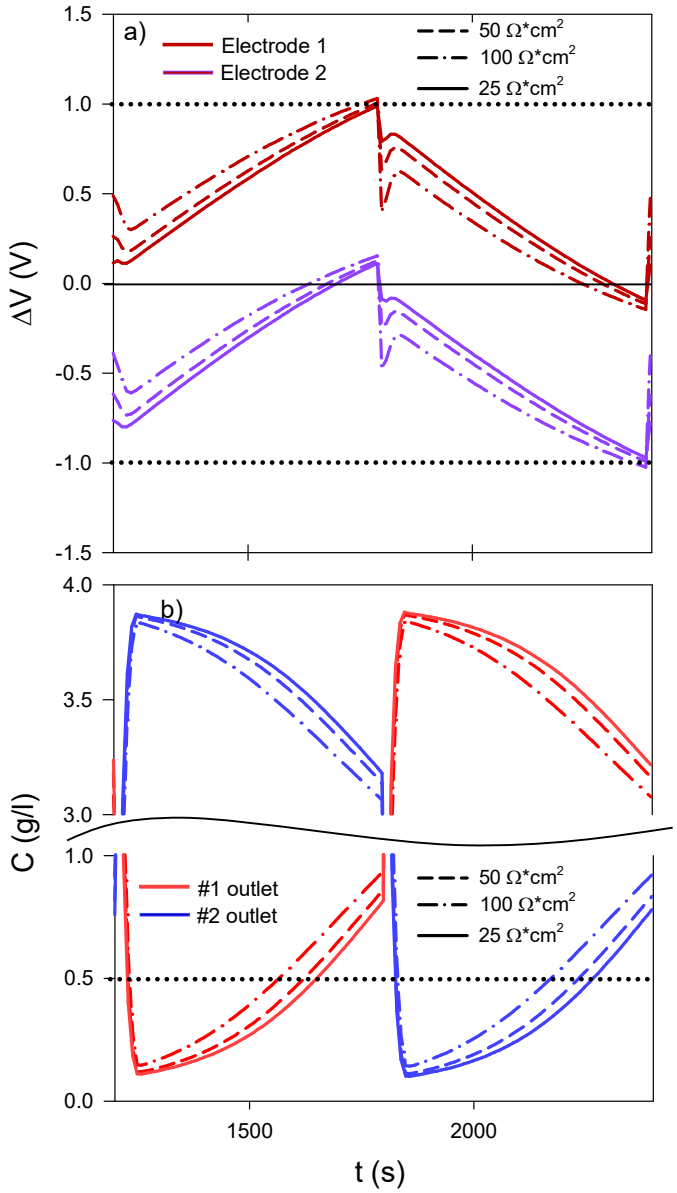

*Figure 12. Simulation results for the comparison of different electrode resistances (25,50 and 100 Ω*cm²) in a single pass CED unit 12.5 cm wide and 80 cm long equipped with 270 µm woven spacers and FUJIFILM capacitive electrodes (RC circuit properties taken from experimental results). Inlet concentration of 2 g/l, linear velocity of 2 cm/s, and ±2 V of applied voltage with polarity switches every 600 s (10 min). a) Electrodes voltage drop vs time, b) outlet concentrations of the two streams vs time.*

5.2.3 Effect of the number of cell pairs

The dynamic effects of capacitive electrodes on process performance (i.e. voltage, current and concentration *vs* time) shown in the previous subsections are also affected by the low number of cell pairs that have been simulated. In fact, an increase in the number of cell pairs can modify the impact that electrode properties have on the overall process. For this reason, the reference case has been replicated with a higher number of cell pairs.

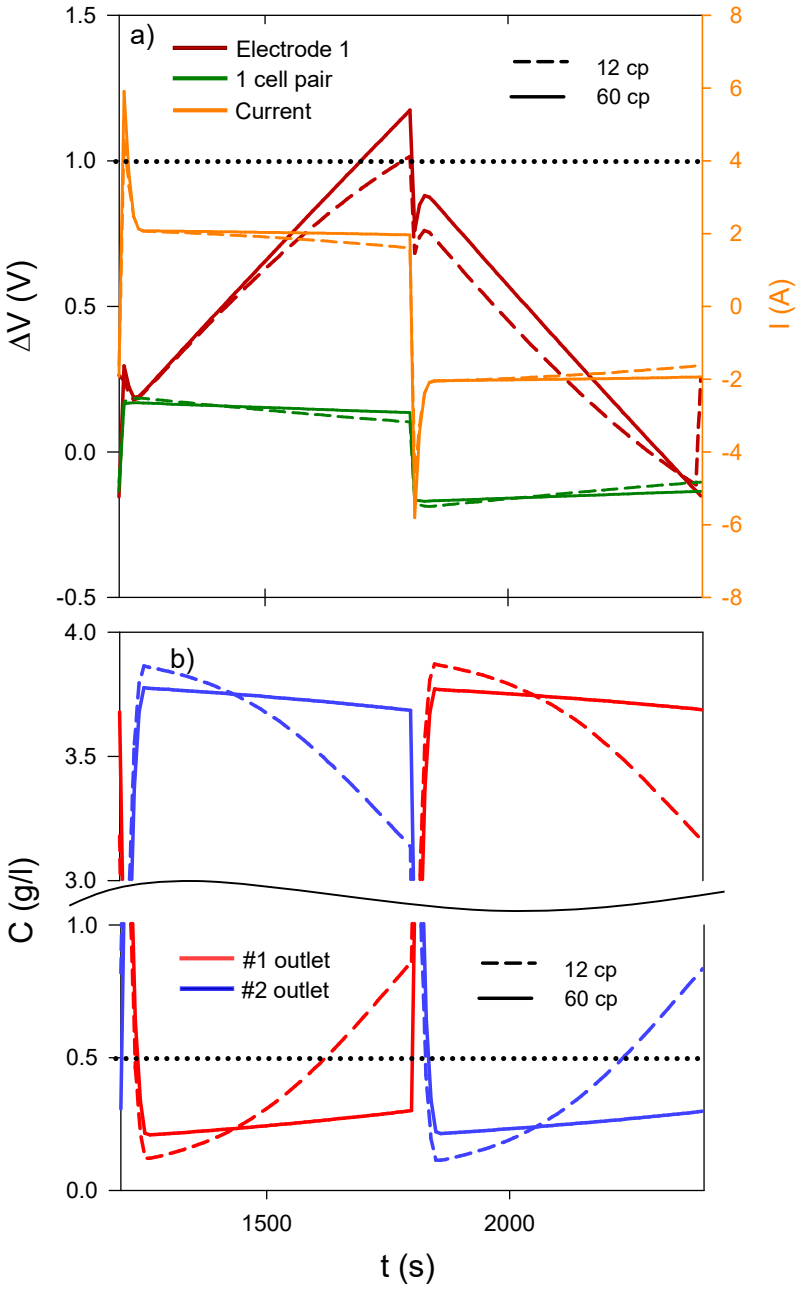

Figure 13. Simulation results showing the effect of a different number of cell pairs (12 and 60) in a single pass CED unit 12.5 cm wide and 80 cm long equipped with 270 µm woven spacers and FUJIFILM capacitive electrodes (RC circuit properties taken from experimental results). Inlet concentration of 2 g/l, linear velocity of 2 cm/s, and fixed voltage (±2 V for 12 cp, ± 9.45 V for 60 cp) with polarity switches every 600 s (10 min). a) Electrode1 and single cell pair voltage drop vs time and current vs time, b) outlet concentrations of the two streams vs time.

Figure 13 shows the comparison between the reference case and a case where 60 cell pairs have been simulated. In order to set a comparable scenario, the total voltage has been fixed in a way that, at the initial condition (i.e. at 0 s), the voltage applied at each cell pair was equal for the two cases. As can be seen, the main effect of increasing the number of cell pairs is a reduction of the slope of the outlet

concentration *vs* time (Figure 13 b). This trend can be explained by the fact that the more the cell pairs the smaller the electrode voltage compared to the voltage of the cell pairs. Consequently, with 60 cell pairs the electrode voltage changes through time almost does not affect the current curve that becomes flatter (orange curve from Figure 13 a) and also does the voltage drop of each cell pair (green curve from Figure 13 a). Of course, current and concentration curves would be perfectly flat for an infinite number of cell pairs. Another interesting consequence of the reduction of the current slope is the increase of the electrodes' voltage slope (only V_{el}^{1} is depicted in Figure 13 a as V_{el}^{2} is qualitatively the same) as they are subjected to a higher average current. As can be deduced from previous discussions (see beginning of Section 5), the two limiting factors that cause the need to reverse polarity in CED operations are the excessive salinity of the dilute stream and the reach of the threshold value of the electrode voltage. Considering the effects on the outlet concentration and on the electrode voltage it can be observed that with increasing number of cell pairs, a progressive shift from the concentration limiting condition to the voltage limiting condition occurs.

6. Conclusions

In this work, the feasibility of the CED process has been proven with both experiments and modelling.

A hierarchical dynamic model for the CED process has been presented for the first time. A single cell pair and the electrodes are separately described in the lowest hierarchy of the model. In particular, capacitive electrodes are modelled as an RC circuit distributed along the direction of the flowing solution. The cell pair and capacitive electrodes are subsequently coupled in the stack model, where the overall variables and performance parameters are calculated. The stack model can then be variously arranged in the highest hierarchy of the plant model.

A set of experiments has been performed with the aim of demonstrating the desalination capability of the CED system. In addition, an experimental characterisation of a set of capacitive electrodes has

been carried out and the collected data have been used as input for the modelled RC circuit as well as to validate the CED model.

Starting from a reference case, the model has been used to assess the effect of different parameters on process performance in conditions closer to real desalination applications. By simulating the same scenario in the presence of an increased capacitance, it was possible to show that the presence of a high capacitance (i.e. 2 F/cm^2) would ensure the feasibility of longer desalination cycles prior to the occurrence of a polarity inversion, thus maintaining the electrode voltage drop below the water splitting threshold and the outlet diluate concentration below the target for a longer time. However, it has been shown that a further increase in the capacitance would unlikely lead to great improvement. A sensitivity analysis for the electrode resistance has been also carried out, demonstrating how 50 $\Omega*cm^2$ is already a low value compared to the Ohmic resistance of the membrane pile that is one order of magnitude higher. Finally, it has been shown how the increase in the number of cell pairs can change the effect of the electrodes, causing a shift in the limiting condition that controls the polarity switch frequency.

Although the *RC circuit* proved its suitability for process modelling, the simplifying assumptions made may affect model reliability in certain conditions. In particular, the presence of faradic reactions can considerably change process outputs at relatively high voltages. Therefore, a future work will comprehensively assess also this aspect.

Acknowledgements

This work has been performed within the REvivED water project (Low energy solutions for drinking water production by a REvival of ElectroDialysis systems). The REvivED water project has received funding from the European Union's Horizon 2020 research and innovation programme under Grant Agreement no. 685579 (www.revivedwater.eu).

List of symbols

A	Membrane area (m^2)
b	Membrane width (m)
C	Concentration (mol/m^3)
c_{el}	Specific capacitance (F/m^2)
D^{IEM}	Salt permeability coefficient of one IEM (m^2/s)
F	Faraday's constant (C/mol)
I	Current (A)
i	Current density (A/m^2)
J_{cond}	Conductive flux ($mol/m^2/s$)
J_{diff}^{IEM}	Diffusive flux across one IEM ($mol/m^2/s$)
J_{tot}	Total salt flux ($mol/m^2/s$)
L	Channel length (m)
L_p	Water permeability ($m^3/Pa/s/m^2$)
M_w	Molecular weight (Kg/mol)
N_{cp}	Number of cell pairs
Q	Volumetric flow rate (m^3/s)
q_{eosm}	Electroosmotic volumetric flux ($m^3/m^2/s$)
q_{osm}^{IEM}	Osmotic volumetric flux across one IEM ($m^3/m^2/s$)
q_w	Total water volumetric flux ($m^3/m^2/s$)
R	Areal electrical resistance (Ωm^2)
R_G	Universal gas constant (J/mol/K)
$t^{counter}$	Counter-ion transport number in the membrane
t	Time (s)
V_{tot}	Overall voltage (V)
V_{cp}	Voltage drop over one cell pair (V)
${V_{el}}^{j}$	Electrode j voltage drop (V)
V_{10cp}	Voltage drop over 10 cell pairs (V)
w	Total water transport number
x	Coordinate in the direction of the main flow

Greek letters

α	Permselectivity
δ	Channel thickness (m)
η	Non-Ohmic voltage drop (V)
π	Osmotic pressure (Pa)
ρ_w	Mass density (Kg/m^3)
σ_{el}	Surface charge density (C/m^2)

Subscripts and superscripts

AEM	Anion-exchange membrane
C	Concentrate
CEM	Cation-exchange membrane
D	Dilute
el	Capacitive electrode
eq	Equivalent circuit
IEM	Ion-exchange membrane
int	Value at the membrane -solution interface, solution side
SOL	Solution (either concentrate or diluate)
tot	Total

References

[1] H. Strathmann, Electrodialysis, a mature technology with a multitude of new applications, Desalination. 264 (2010) 268–288. doi:10.1016/j.desal.2010.04.069.

[2] A. Campione, L. Gurreri, M. Ciofalo, G. Micale, A. Tamburini, A. Cipollina, Electrodialysis for water desalination: A critical assessment of recent developments on process fundamentals, models and applications, Desalination. 434 (2018) 121–160. doi:10.1016/j.desal.2017.12.044.

[3] A.H. Galama, M. Saakes, H. Bruning, H.H.M. Rijnaarts, J.W. Post, Seawater predesalination with electrodialysis, Desalination. 342 (2014) 61–69. doi:10.1016/j.desal.2013.07.012.

[4] B. Van der Bruggen, Advances in electrodialysis for water treatment, in: A. Basile, A. Cassano, N.K. Rastogi (Eds.), Adv. Membr. Technol. Water Treat. Mater. Process. Appl., Woodhead Publishing, 2015: pp. 185–203. doi:10.1016/B978-1-78242-121-4.00006-X.

[5] J.H. Barber, R. MacDonald, H. Yang, W. Lu, Capacitive carbon electrodes for electrodialysis reversal applications, in: American Water Works Association, 2014.

[6] C. Wei, Y. Du, W. Cai, R. Xiong, L. Cao, Non-faraday based systems, devices and methods for removing ionic species from liquid, US20110042219A1, 2011. https://patents.google.com/patent/US20110042219 (accessed

June 25, 2018).

[7] D.A. Vermaas, S. Bajracharya, B.B. Sales, M. Saakes, B. Hamelers, K. Nijmeijer, Clean energy generation using capacitive electrodes in reverse electrodialysis, Energy Environ. Sci. 6 (2013) 643–651. doi:10.1039/C2EE23562E.

[8] P. Ratajczak, M.E. Suss, F. Kaasik, F. Béguin, Carbon electrodes for capacitive technologies, Energy Storage Mater. 16 (2019) 126–145. doi:10.1016/j.ensm.2018.04.031.

[9] P.M. Biesheuvel, M.Z. Bazant, Nonlinear dynamics of capacitive charging and desalination by porous electrodes, Phys. Rev. E. 81 (2010) 031502. doi:10.1103/PhysRevE.81.031502.

[10] M.E. Suss, T.F. Baumann, M.A. Worsley, K.A. Rose, T.F. Jaramillo, M. Stadermann, J.G. Santiago, Impedance-based study of capacitive porous carbon electrodes with hierarchical and bimodal porosity, J. Power Sources. 241 (2013) 266–273. doi:10.1016/J.JPOWSOUR.2013.03.178.

[11] G. Wang, L. Zhang, J. Zhang, A review of electrode materials for electrochemical supercapacitors, Chem. Soc. Rev. 41 (2012) 797–828. doi:10.1039/C1CS15060J.

[12] E. Frackowiak, F. Béguin, Carbon materials for the electrochemical storage of energy in capacitors, Carbon N. Y. 39 (2001) 937–950. doi:10.1016/S0008-6223(00)00183-4.

[13] Y. Ding, J. Zhu, C. Wang, B. Dai, Y. Li, Y. Qin, F. Xu, Q. Peng, Z. Yang, J. Bai, W. Cao, Y. Yuan, Y. Li, Multifunctional three-dimensional graphene nanoribbons composite sponge, Carbon N. Y. 104 (2016) 133–140. doi:10.1016/J.CARBON.2016.03.058.

[14] E. Castillo-Martínez, J. Carretero-González, J. Sovich, M.D. Lima, High temperature structural transformations of few layer graphene nanoribbons obtained by unzipping carbon nanotubes, J. Mater. Chem. A. 2 (2014) 221–228. doi:10.1039/C3TA13292G.

[15] X. Zhou, L. Yu, X.-Y. Yu, X.W.D. Lou, Encapsulating Sn Nanoparticles in Amorphous Carbon Nanotubes for Enhanced Lithium Storage Properties, Adv. Energy Mater. 6 (2016) 1601177. doi:10.1002/aenm.201601177.

[16] G. Xiong, P. He, Z. Lyu, T. Chen, B. Huang, L. Chen, T.S. Fisher, Bioinspired leaves-on-branchlet hybrid carbon nanostructure for supercapacitors, Nat. Commun. 9 (2018) 790. doi:10.1038/s41467-018-03112-3.

[17] E.S. Snow, F.K. Perkins, E.J. Houser, S.C. Badescu, T.L. Reinecke, Chemical Detection with a Single-Walled Carbon Nanotube Capacitor, Science (80-.). 307 (2005) 1942–1945. doi:10.1126/science.1109128.

[18] C. Portet, G. Yushin, Y. Gogotsi, Electrochemical performance of carbon onions, nanodiamonds, carbon black and multiwalled nanotubes in electrical double layer capacitors, Carbon N. Y. 45 (2007) 2511–2518. doi:10.1016/J.CARBON.2007.08.024.

[19] M.E. Plonska-Brzezinska, L. Echegoyen, Carbon nano-onions for supercapacitor electrodes: recent developments and applications, J. Mater. Chem. A. 1 (2013) 13703. doi:10.1039/c3ta12628e.

[20] J. García-Martínez, K. Li, Mesoporous Zeolites, Wiley-VCH Verlag GmbH & Co. KGaA, Weinheim, Germany, 2015. doi:10.1002/9783527673957.

[21] N. Boukmouche, N. Azzouz, L. Bouchama, J.P. Chopart, Y. Bouznit, Activated carbon derived from marine Posidonia Oceanica for electric energy storage, Arab. J. Chem. 7 (2014) 347–354. doi:10.1016/j.arabjc.2012.12.010.

[22] F. Béguin, V. Presser, A. Balducci, E. Frackowiak, Carbons and Electrolytes for Advanced Supercapacitors, Adv. Mater. 26 (2014) 2219–2251. doi:10.1002/adma.201304137.

[23] H.F. Stoeckli, F. Kraehenbuehl, The external surface of microporous carbons, derived from adsorption and immersion studies, Carbon N. Y. 22 (1984) 297–299. doi:10.1016/0008-6223(84)90174-X.

[24] T. Alencherry, N. A.R., S. Ghosh, J. Daniel, V. R., Effect of increasing electrical conductivity and hydrophilicity on the electrosorption capacity of activated carbon electrodes for capacitive deionization, Desalination. 415 (2017) 14–19. doi:10.1016/J.DESAL.2017.04.001.

[25] L. Zou, G. Morris, D. Qi, Using activated carbon electrode in electrosorptive deionisation of brackish water, Desalination. 225 (2008) 329–340. doi:10.1016/J.DESAL.2007.07.014.

[26] C.-H. Hou, C.-Y. Huang, A comparative study of electrosorption selectivity of ions by activated carbon electrodes in capacitive deionization, Desalination. 314 (2013) 124–129. doi:10.1016/J.DESAL.2012.12.029.

[27] J.Y. Hwang, M. Li, M.F. El-Kady, R.B. Kaner, Next-Generation Activated Carbon Supercapacitors: A Simple Step in Electrode Processing Leads to Remarkable Gains in Energy Density, Adv. Funct. Mater. 27 (2017)

1605745. doi:10.1002/adfm.201605745.

[28] M. Olivares-Marín, J.A. Fernández, M.J. Lázaro, C. Fernández-González, A. Macías-García, V. Gómez-Serrano, F. Stoeckli, T.A. Centeno, Cherry stones as precursor of activated carbons for supercapacitors, Mater. Chem. Phys. 114 (2009) 323–327. doi:10.1016/J.MATCHEMPHYS.2008.09.010.

[29] I. Villar, S. Roldan, V. Ruiz, M. Granda, C. Blanco, R. Menéndez, R. Santamaría, Capacitive Deionization of NaCl Solutions with Modified Activated Carbon Electrodes †, Energy & Fuels. 24 (2010) 3329–3333. doi:10.1021/ef901453q.

[30] C. Vix-Guterl, E. Frackowiak, K. Jurewicz, M. Friebe, J. Parmentier, F. Béguin, Electrochemical energy storage in ordered porous carbon materials, Carbon N. Y. 43 (2005) 1293–1302. doi:10.1016/J.CARBON.2004.12.028.

[31] A.G. Pandolfo, A.F. Hollenkamp, Carbon properties and their role in supercapacitors, J. Power Sources. 157 (2006) 11–27. doi:10.1016/J.JPOWSOUR.2006.02.065.

[32] F. Liu, O. Coronell, D.F. Call, Electricity generation using continuously recirculated flow electrodes in reverse electrodialysis, J. Power Sources. 355 (2017) 206–210. doi:10.1016/J.JPOWSOUR.2017.04.061.

[33] J.M. Paz-Garcia, O. Schaetzle, P.M. Biesheuvel, H.V.M. Hamelers, Energy from CO2 using capacitive electrodes – Theoretical outline and calculation of open circuit voltage, J. Colloid Interface Sci. 418 (2014) 200–207. doi:10.1016/J.JCIS.2013.11.081.

[34] D. Brogioli, Extracting Renewable Energy from a Salinity Difference Using a Capacitor, Phys. Rev. Lett. 103 (2009) 058501. doi:10.1103/PhysRevLett.103.058501.

[35] Y.A.C. Jande, W.S. Kim, Desalination using capacitive deionization at constant current, Desalination. 329 (2013) 29–34. doi:10.1016/J.DESAL.2013.08.023.

[36] Y. Salamat, C.H. Hidrovo, A parametric study of multiscale transport phenomena and performance characteristics of capacitive deionization systems, Desalination. 438 (2018) 24–36. doi:10.1016/J.DESAL.2018.03.022.

[37] Z. Chen, H. Zhang, C. Wu, L. Luo, C. Wang, S. Huang, H. Xu, A study of the effect of carbon characteristics on capacitive deionization (CDI) performance, Desalination. 433 (2018) 68–74. doi:10.1016/J.DESAL.2017.11.036.

[38] O.N. Demirer, R.M. Naylor, C.A. Rios Perez, E. Wilkes, C. Hidrovo, Energetic performance optimization of a capacitive deionization system operating with transient cycles and brackish water, Desalination. 314 (2013) 130–138. doi:10.1016/J.DESAL.2013.01.014.

[39] J. Ma, C. He, D. He, C. Zhang, T.D. Waite, Analysis of capacitive and electrodialytic contributions to water desalination by flow-electrode CDI, Water Res. 144 (2018) 296–303. doi:10.1016/J.WATRES.2018.07.049.

[40] A. Rommerskirchen, Y. Gendel, M. Wessling, Single module flow-electrode capacitive deionization for continuous water desalination, Electrochem. Commun. 60 (2015) 34–37. doi:10.1016/J.ELECOM.2015.07.018.

[41] A. Rommerskirchen, B. Ohs, K.A. Hepp, R. Femmer, M. Wessling, Modeling continuous flow-electrode capacitive deionization processes with ion-exchange membranes, J. Memb. Sci. 546 (2018) 188–196. doi:10.1016/J.MEMSCI.2017.10.026.

[42] SUEZ, Carbon Electrodes for EDR, (2013). https://my.suezwatertechnologies.com/WTSCustomerPortal/s/content-download?DN=%2Fdocuments%2FFact+Sheets_Cust%2FAmericas%2FEnglish%2FFSelEDRCarbonElectrode_EN.pdf (accessed July 29, 2019).

[43] J.A. Wesselingh, P. Vonk, G. Kraaijeveld, Exploring the Maxwell-Stefan description of ion exchange, Chem. Eng. J. Biochem. Eng. J. 57 (1995) 75–89. doi:10.1016/0923-0467(94)02932-6.

[44] H.J. Lee, F. Sarfert, H. Strathmann, S.H. Moon, Designing of an electrodialysis desalination plant, Desalination. 142 (2002) 267–286. doi:10.1016/S0011-9164(02)00208-4.

[45] M. Sadrzadeh, A. Kaviani, T. Mohammadi, Mathematical modeling of desalination by electrodialysis, Desalination. 206 (2007) 538–546. doi:10.1016/j.desal.2006.04.062.

[46] G. Kraaijeveld, V. Sumberova, S. Kuindersma, H. Wesselingh, Modelling electrodialysis using the Maxwell-Stefan description, Chem. Eng. J. Biochem. Eng. J. 57 (1995) 163–176. doi:10.1016/0923-0467(94)02940-7.

[47] R.K. McGovern, S.M. Zubair, J.H. Lienhard V, The cost effectiveness of electrodialysis for diverse salinity applications, Desalination. 348 (2014) 57–65. doi:10.1016/j.desal.2014.06.010.

[48] M. Fidaleo, M. Moresi, Optimal strategy to model the electrodialytic recovery of a strong electrolyte, J. Memb. Sci. 260 (2005) 90–111. doi:10.1016/j.memsci.2005.01.048.

[49] N.C. Wright, S.R. Shah, S.E. Amrose, A.G. Winter, A robust model of brackish water electrodialysis desalination with experimental comparison at different size scales, Desalination. 443 (2018) 27–43. doi:10.1016/J.DESAL.2018.04.018.

[50] Z. Zourmand, F. Faridirad, N. Kasiri, T. Mohammadi, Mass transfer modeling of desalination through an electrodialysis cell, Desalination. 359 (2015) 41–51. doi:10.1016/j.desal.2014.12.008.

[51] K. Tado, F. Sakai, Y. Sano, A. Nakayama, An analysis on ion transport process in electrodialysis desalination, Desalination. 378 (2016) 60–66. doi:10.1016/j.desal.2015.10.001.

[52] R. Enciso, J.A. Delgadillo, O. Domínguez, I. Rodríguez-Torres, Analysis and validation of the hydrodynamics of an electrodialysis cell using computational fluid dynamics, Desalination. 408 (2017) 127–132. doi:10.1016/j.desal.2017.01.015.

[53] M. Tedesco, H.V.M. Hamelers, P.M. Biesheuvel, Nernst-Planck transport theory for (reverse) electrodialysis: I. Effect of co-ion transport through the membranes, J. Memb. Sci. 510 (2016) 370–381.

[54] M. Tedesco, H.V.M. Hamelers, P.M. Biesheuvel, Nernst-Planck transport theory for (reverse) electrodialysis: II. Effect of water transport through ion-exchange membranes, J. Memb. Sci. 531 (2017) 172–182. doi:10.1016/j.memsci.2017.02.031.

[55] Y. Tanaka, Concentration polarization in ion-exchange membrane electrodialysis: The events arising in an unforced flowing solution in a desalting cell, J. Memb. Sci. 244 (2004) 1–16. doi:10.1016/j.memsci.2004.02.041.

[56] P.N. Pintauro, D.N. Bennion, Mass transport of electrolytes in membranes. 1. Development of mathematical transport model, Ind. Eng. Chem. Fundam. 23 (1984) 230–234. http://www.scopus.com/inward/record.url?eid=2-s2.0-0021425029&partnerID=tZOtx3y1.

[57] M. Andelman, Flow through capacitor basics, Sep. Purif. Technol. 80 (2011) 262–269. doi:10.1016/j.seppur.2011.05.004.

[58] Y. Qu, P.G. Campbell, L. Gu, J.M. Knipe, E. Dzenitis, J.G. Santiago, M. Stadermann, Energy consumption analysis of constant voltage and constant current operations in capacitive deionization, Desalination. 400 (2016) 18–24. doi:10.1016/J.DESAL.2016.09.014.

[59] A. Hemmatifar, M. Stadermann, J.G. Santiago, Two-Dimensional Porous Electrode Model for Capacitive Deionization, J. Phys. Chem. C. 119 (2015) 24681–24694. doi:10.1021/acs.jpcc.5b05847.

[60] J. Newman, W. Tiedemann, Porous-electrode theory with battery applications, AIChE J. 21 (1975) 25–41. doi:10.1002/aic.690210103.

[61] A.M. Johnson, J. Newman, Desalting by Means of Porous Carbon Electrodes, J. Electrochem. Soc. 118 (1971) 510. doi:10.1149/1.2408094.

[62] J.S. Newman, Electrochemical Systems, second, Prentice Hall, Englewood Cliffs, 1991.

[63] P.M. Biesheuvel, Y. Fu, M.Z. Bazant, Diffuse charge and Faradaic reactions in porous electrodes, Phys. Rev. E. 83 (2011) 061507. doi:10.1103/PhysRevE.83.061507.

[64] M. La Cerva, M. Di Liberto, L. Gurreri, A. Tamburini, A. Cipollina, G. Micale, M. Ciofalo, Coupling CFD with simplified 1-D models to predict the performance of reverse electrodialysis stacks, J. Memb. Sci. 541 (2017) 595–610. doi:10.1016/j.memsci.2017.07.030.

[65] S. Pawlowski, V. Geraldes, J.G. Crespo, S. Velizarov, Computational fluid dynamics (CFD) assisted analysis of profiled membranes performance in reverse electrodialysis, J. Memb. Sci. 502 (2016) 179–190.

[66] M. Tedesco, A. Cipollina, A. Tamburini, I.D.L. Bogle, G. Micale, A simulation tool for analysis and design of reverse electrodialysis using concentrated brines, Chem. Eng. Res. Des. 93 (2015) 441–456. doi:10.1016/j.cherd.2014.05.009.

[67] K.M. Chehayeb, D.M. Farhat, K.G. Nayar, J.H. Lienhard, Optimal design and operation of electrodialysis for brackish-water desalination and for high-salinity brine concentration, Desalination. 420 (2017) 167–182. doi:10.1016/j.desal.2017.07.003.

[68] N.A.A. Qasem, B.A. Qureshi, S.M. Zubair, Improvement in design of electrodialysis desalination plants by considering the Donnan potential, Desalination. 441 (2018) 62–76. doi:10.1016/j.desal.2018.04.023.

[69] B.A. Qureshi, S.M. Zubair, Design of electrodialysis desalination plants by considering dimensionless groups and variable equivalent conductivity, Desalination. 430 (2018) 197–207. doi:10.1016/j.desal.2017.12.030.

[70] A. Campione, A. Cipollina, I.D.L. Bogle, L. Gurreri, A. Tamburini, M. Tedesco, G. Micale, A hierarchical model

for novel schemes of electrodialysis desalination, Desalination. 465 (2019) 79–93. doi:10.1016/j.desal.2019.04.020.

[71] R. de Levie, On porous electrodes in electrolyte solutions: I. Capacitance effects, Electrochim. Acta. 8 (1963) 751–780. doi:10.1016/0013-4686(63)80042-0.

[72] R. Kötz, M. Carlen, Principles and applications of electrochemical capacitors, Electrochim. Acta. 45 (2000) 2483–2498. doi:10.1016/S0013-4686(00)00354-6.

[73] P.M. Biesheuvel, H.V.M. Hamelers, M.E. Suss, Theory of Water Desalination by Porous Electrodes with Immobile Chemical Charge, Colloids Interface Sci. Commun. 9 (2015) 1–5. doi:10.1016/J.COLCOM.2015.12.001.

[74] E.N. Guyes, A.N. Shocron, A. Simanovski, P.M. Biesheuvel, M.E. Suss, A one-dimensional model for water desalination by flow-through electrode capacitive deionization, Desalination. 415 (2017) 8–13. doi:10.1016/J.DESAL.2017.03.013.

[75] L. Gurreri, A. Tamburini, A. Cipollina, G. Micale, M. Ciofalo, CFD prediction of concentration polarization phenomena in spacer-filled channels for reverse electrodialysis, J. Memb. Sci. 468 (2014) 133–148. doi:10.1016/j.memsci.2014.05.058.

[76] L. Gurreri, A. Tamburini, A. Cipollina, G. Micale, M. Ciofalo, Flow and mass transfer in spacer-filled channels for reverse electrodialysis: a CFD parametrical study, J. Memb. Sci. 497 (2016) 300–317. doi:10.1016/j.memsci.2015.09.006.

[77] L. Gurreri, M. Ciofalo, A. Cipollina, A. Tamburini, W. Van Baak, G. Micale, CFD modelling of profiled-membrane channels for reverse electrodialysis, Desalin. Water Treat. 55 (2015) 1–20. doi:10.1080/19443994.2014.940651.

[78] L. Gurreri, A. Tamburini, A. Cipollina, G. Micale, M. Ciofalo, Pressure drop at low reynolds numbers in woven-spacer-filled channels for membrane processes: CFD prediction and experimental validation, Desalin. Water Treat. 61 (2017) 170–182. doi:10.5004/dwt.2016.11279.

[79] D.L. Chapman, LI. A contribution to the theory of electrocapillarity, London, Edinburgh, Dublin Philos. Mag. J. Sci. 25 (1913) 475–481. doi:10.1080/14786440408634187.

SUPPLEMENTARY MATERIAL

Water desalination by capacitive electrodialysis: experiments and modelling

Antonino Campione[a], Andrea Cipollina[a,], Erwin Toet[b], Luigi Gurreri[a], I. David L. Bogle[c], Giorgio Micale[a]*

[a] *Dipartimento di Ingegneria, Università degli Studi di Palermo, viale delle Scienze Ed.6, 90128 Palermo, Italy*

[b] *FUJIFILM Manufacturing Europe, Oudenstaart 1, 5000 LJ Tilburg, The Netherlands.*

[c]*Centre for Process Systems Engineering, Department of Chemical Engineering, University College London, Torrington Place, London WC1E 7JE, UK.*

[*]*Corresponding Author (A. Cipollina):* andrea.cipollina@unipa.it

Electrodialysis cell pair model description

This section is intended to give a more detailed description of the lower hierarchy model of the cell pair, briefly described in the modelling section of the paper. All the equations involved, including the ones already presented in the main paper, will be shown.

At the scale of the cell pair, mass balances, transport phenomena, solutions thermodynamics and electrical parameters are described.

Different transport phenomena take place inside the cell pair, causing both salt and water to move through membranes. The main salt transport mechanism is the conductive flux, which is proportional to the ionic current and is associated to the external applied voltage. In a general position along the length of the cell pair, it can be calculated as:

$$J_{cond}(x,t) = [t_{CEM}^{counter} - (1 - t_{AEM}^{counter})] \frac{i\,(x,t)}{F} \tag{13}$$

where i is the current density, F is the Faraday constant, and $t_{CEM}^{counter}$ and $t_{AEM}^{counter}$ are the transport numbers of the counter-ions inside the IEMs, directly linked with the membrane permselectivity using the following expression [1]:

$$\alpha_{IEM} = \frac{t_{IEM}^{counter} - t_{SOL}^{counter}}{t_{SOL}^{co}} \tag{14}$$

where $t_{SOL}^{counter}$ and t_{SOL}^{co} are the transport numbers of counter-ion and co-ion in solution, and the subscript IEM indicates that, using the relevant values, the expression is valid either for AEM or CEM. It is worth noting that the term $[t_{CEM}^{counter} - (1 - t_{AEM}^{counter})]$ in eq. (13) is representative of the

non-ideal permselectivity of the membranes, as it accounts for the conductive co-ion transport through IEMs that in practice results in a drop of the salt removal efficiency of the system.

In addition to the effects on the conductive flux, another consequence of the non-perfect membrane selectivity is the occurrence of a back-diffusive salt flux driven by the salt concentration difference between the channels, which, for a single membrane, can be written as:

$$J_{diff}^{IEM}(x,t) = -\frac{D^{IEM}}{\delta^{IEM}}\left(C_C{}^{int,IEM}(x,t) - C_D{}^{int,IEM}(x,t)\right) \quad (15)$$

where D is the salt permeability coefficient through the IEM, δ is the thickness of IEM and C^{int} is the salt concentration in solution at the interface with the membrane. Subscripts C and D refer to concentrate and diluate respectively and the superscript IEM indicates that, using the relevant values, the expression is valid for both AEM and CEM. The overall diffusive flux can be written as the sum of the fluxes through the two membranes.

Also water molecules can move through the membranes. Water transport can be attributed to two phenomena: osmosis and electroosmosis. The first transport mechanism is caused by the transmembrane osmotic pressure difference and can be expressed as:

$$q_{osm}^{IEM}(x,t) = L_p^{IEM}\left(\pi_C^{IEM} - \pi_D^{IEM}\right) \quad (16)$$

i.e.

$$q_{osm}^{IEM}(x,t) = L_p^{IEM}\left[\nu R_G T\left(\varphi_C^{IEM} C_C{}^{int,IEM}(x,t) - \varphi_C^{IEM} C_D{}^{int,IEM}(x,t)\right)\right] \quad (17)$$

where L_p is the water permeability coefficient of IEMs and π is the osmotic pressure that can be related to the van 't Hoff coefficient (ν), the osmotic coefficient (φ) and the solution concentration. Pitzer's correlations are used to estimate osmotic coefficients [2,3]:

$$\varphi - 1 = -A_1 \frac{\sqrt{m}}{1 + b'\sqrt{m}} + mB^{\varphi} + m^2 C^{\varphi} \quad (18)$$

$$B^{\varphi} = \beta^{(0)} + \beta^{(1)} e^{-\alpha\sqrt{m}} \quad (19)$$

where A_1 is the modified Debye-Huckel constant (0.3915 at 25 °C), $b'$is a correlation constant equal to 1.2, m is the molality of the electrolyte, α is a fixed constant with a value of 2 (kg/mol)$^{1/2}$, $\beta^{(0)}$, $\beta^{(1)}$, $C^{\varphi}$are functions of the nature of the electrolyte and amount to 0.06743, 0.3301 and 0.00263, respectively, for NaCl. As for the diffusive flux, the total osmotic flux is the sum of the fluxes on the two membranes.

The second water transport mechanism, electroosmosis, is the water flux coupled with the ions movement due to two main contributions: the water molecules of the solvation shell and the water flux dragged by the momentum arising on the slip-plane between the solvation shell and the solvent [4,5]. Generally, electroosmosis can be expressed as a function of the overall salt flux:

$$q_{eosm}(x,t) = \frac{w\, J_{tot}(x,t) M_w}{\rho_w} \quad (20)$$

where J_{tot} is the sum of the diffusive (of both AEM and CEM) and the migrative salt flux and w is the total water transport number, defined as the sum of the water transport number relative to each

ion. In ref. [4], Wilson reports that for most membranes the ionic transport numbers are close to the primary hydration numbers. Thus, for a NaCl solution a value of 12 moles per equivalent of transported salt can be assumed.

The model computes distributions over the dimension of the channel length and time. Bulk concentration and flowrate distributions inside the channels are described through differential mass balance equations that, in the case of co-current flow and negligible changes in the solutions density, are:

$$b\delta_{SOL}\frac{\partial C_{SOL}(x,t)}{\partial t}+\frac{\partial Q_{SOL}(x,t)C_{SOL}(x,t)}{\partial x}=\pm b\,J_{tot}(x,t) \tag{21}$$

$$\frac{d\,Q_{SOL}(x,t)}{dx}=\pm\,b\,q_w(x,t) \tag{22}$$

where Q represents the local volumetric flow rate, b the channel width and q_w the local overall volumetric water flux (i.e. the sum of osmotic and electroosmotic fluxes). The signs + and – refers to the concentrate and the diluate respectively. It is worth noting that in the overall mass balance equation, the accumulation term (time-derivative of total mass in the control volume) is null due to the assumption of incompressible fluid flowing through a constant cross-section (i.e. constant volume) channel.

A crucial aspect of ED process modelling is to relate the ionic current to the applied voltage. The voltage drop over a cell pair (V_{cp}) is calculated as:

$$V_{cp}(x,t)=\,\eta\,(x,t)+R_{tot}(x,t)i(x,t) \tag{23}$$

where η is the non-ohmic voltage drop associated to the back electromotive force (diffusion potentials are not taken into account), i is the current density, R_{tot} is the total areal ohmic resistance of cell pair that can be calculated as the sum of the four components in series

$$R_{tot}(x,t)=\,R_{CEM}(x,t)+\,R_{AEM}(x,t)+R_C(x,t)+\,R_D(x,t) \tag{24}$$

where R_{CEM} and R_{AEM} represents the resistance of IEMs. R_C and R_D are the resistance of concentrate and diluate respectively, and, neglecting the ohmic contribution of the diffusion boundary layers, can be generally expressed as:

$$R_{SOL}(x,t)=f_{sSOL}\,\frac{\delta_{SOL}}{\Lambda_{SOL}(x,t)\;C_{SOL}(x,t)} \tag{25}$$

with δ being the compartment thickness, f_s the shadow factor, which accounts for the resistance increase due to the presence of a non-conductive spacer [6] and Λ the equivalent conductivity. The subscript SOL refers to the generic solution, thus making the equation valid for both concentrate and diluate resistances by using the relevant parameters. For a NaCl salt solution, the equivalent conductivity can be estimated by the correlation of Islam et al. [7]:

$$\Lambda(x,t)=\,\left[\Lambda^0-\frac{B'_1(C)\sqrt{C}}{1+B'(C)\;a\sqrt{C}}\right]\left[1-\frac{B'_2(C)\sqrt{C}}{1+B'(C)\;a\sqrt{C}}F'(C)\right] \tag{26}$$

$$B^{'}(C)=50.29\cdot10^{8}/(\varepsilon T)^{1/2} \tag{27}$$

$$B'_1(C) = 82.5/[\eta(\varepsilon T)^{1/2}] \quad (28)$$

$$B'_2(C) = 8.204 \cdot 10^5/(\varepsilon T)^{3/2} \quad (29)$$

$$F'(C) = \frac{\left[exp\left(0.2929\, B'\, C^{1/2}a\right) - 1\right]}{\left(0.2929\, B'\, cC^{1/2}a\right)} \quad (30)$$

where Λ^0 is the equivalent conductivity at infinite dilution, C is the molar concentration, η is the viscosity, ε the dielectric constant and T the electrolyte solution temperature and $a = 3.79\, A^o$ for NaCl. The main advantage of using this correlation is that it can reliably predict the conductivity even at high ionic strength (i.e. with concentrated brines).

The shadow factor is generally a function of the geometrical characteristics of the spacer. Therefore, it is usually calculated as a function of the channel porosity [8,9], open area [6], or both [10,11]. The porosity represents the fraction of channel volume occupied by the liquid, while the open area represents the free fraction of membrane area projected in the direction perpendicular to membranes. Values for the open area typically range between 40-60% [6]. In this study, the shadow factor for the simulated spacer has been calculated by finite-volume simulations (solving the Laplace equation for the electric potential), resulting in a value that is close to the reciprocal of the average of porosity and open area, and is in agreement with experimental findings [12].

It is known that membrane resistance is influenced by solution concentration [13–15]. According to the experimental data by Galama et al. [13], membrane resistance appears to be generally influenced by diluate solution concentration. Based on those findings, the following trend can be attributed to membrane resistance:

$$R_{IEM}(x,t) = R_{IEM}^{HIGH} + \frac{a}{C(x,t)^n} \quad (31)$$

where R_{IEM}^{HIGH}, a and n and are constants with value of 7×10^{-3} and 1.25 respectively for a resistance expressed as ohm*m^2. In this specific case, R_{IEM}^{HIGH} has been taken equal to the value of the resistance measured at the standard concentration of 0.5 M NaCl. The values of the other constants are obtained by assuming the same trend of membrane resistance against the diluate concentration reported in Galama's work [13].

The non-ohmic contribution of the voltage drop (η) is the sum of the membrane potentials that are established within all cell pairs due to the different salt concentration between flowing solutions. A simplified expression of the membrane potential can be derived from the Teorell-Meyer-Sievers theory [16,17]. Taking also into account concentration polarisation effects, the non-ohmic drop can be calculated as follows:

$$\eta(x,t) = \eta_{CEM}(x,t) + \eta_{AEM}(x,t) \quad (32)$$

$$\eta_{IEM}(x,t) = \alpha_{IEM}\frac{R_G T}{F} ln\left[\frac{\gamma_C^{int,IEM}(x,t)\, C_C^{int,IEM}}{\gamma_D^{int,IEM}(x,t)\; C_D^{int,IEM}}\right] \quad (33)$$

where α_{IEM} is the permselectivity of one IEM, γ^{int} and C^{int} represent the activity coefficient and the salt concentration, respectively, at the membrane-solution interface. Similarly to osmotic

coefficients, the Pitzer model can be used to estimate the average activity coefficient of salt in solution ($\gamma_{\pm}$) [2,3]:

$$ln\gamma_{\pm} = -A_1 \left[\frac{\sqrt{m}}{1+b'\sqrt{m}} + \frac{2}{b'}\ln\left(1+b'\sqrt{m}\right)\right] + mB^{\gamma} + m^2C^{\gamma} \quad (34)$$

$$B^{\gamma} = 2\beta^{(0)} + 2\beta^{(1)}\left[1-\left(1+\alpha\, m^{\frac{1}{2}} - \frac{\alpha^2 m}{2}\right) exp\left(-\alpha\, m^{\frac{1}{2}}\right)\right]/\alpha^2 m \quad (35)$$

$$C^{\gamma} = \frac{3}{2}\, C^{\varphi} \quad (36)$$

The salt concentrations at the solution-membrane interfaces are estimated as functions of the current density and the Sherwood number. In particular, neglecting the salt back-diffusion, eq. (15), the interface salt concentrations (solution side) appearing in eq. (33) can be estimated by the following relations [18,19]:

$$C_C^{int,IEM}(x,t) = C_C(x,t) + \frac{\left(t_{IEM}^{counter} - t_C^{counter}\right) i(x,t)}{F\, Sh_C^{IEM}(x,t)} \frac{d_C^{eq}}{D_C} \quad (37)$$

$$C_D^{int,IEM}(x,t) = C_D(x,t) - \frac{\left(t_{IEM}^{counter} - t_D^{counter}\right) i(x,t)}{F Sh_D^{IEM}(x,t)} \frac{d_D^{eq}}{D_D} \quad (38)$$

where Sh is the Sherwood number, D is the salt diffusion in solution and d_{eq} is the equivalent diameter, here assumed equal to two times the channel thickness. Sherwood numbers, in turn, are computed through correlations obtained by 3-D CFD simulations for various spacer or profiled membrane geometries [20–22].

References

[1] H. Strathmann, Ion-exchange membrane separation processes, First ed., Elsevier, Amsterdam, 2004.

[2] K.S. Pitzer, Thermodynamics of electrolytes. I. Theoretical basis and general equations, J. Phys. Chem. 77 (1973) 268–277. doi:10.1021/j100621a026.

[3] C.F. Weber, Calculation of Pitzer Parameters at High Ionic Strengths, Ind. Eng. Chem. Res. 39 (2000) 4422–4426. doi:10.1021/ie000411o.

[4] J.R. Wilson, Demineralization by electrodialysis, Butterworths Scientific Publications, 1960.

[5] A. Despić, G.J. Hills, Electro-osmosis in charged membranes. The determination of primary solvation numbers, Discuss. Faraday Soc. 21 (1956) 150. doi:10.1039/df9562100150.

[6] M. Tedesco, A. Cipollina, A. Tamburini, I.D.L. Bogle, G. Micale, A simulation tool for analysis and design of reverse electrodialysis using concentrated brines, Chem. Eng. Res. Des. 93 (2015) 441–456. doi:10.1016/j.cherd.2014.05.009.

[7] S.S. Islam, R.L. Gupta, K. Ismail, Extension of the Falkenhagen-Leist-Kelbg equation to the electrical conductance of concentrated aqueous electrolytes, J. Chem. Eng. Data. 36 (1991) 102–104. doi:10.1021/je00001a031.

[8] S. Pawlowski, V. Geraldes, J.G. Crespo, S. Velizarov, Computational fluid dynamics (CFD) assisted analysis of profiled membranes performance in reverse electrodialysis, J. Memb. Sci. 502 (2016) 179–190.

[9] A.M. Weiner, R.K. McGovern, J.H. Lienhard V, Increasing the power density and reducing the levelized cost of electricity of a reverse electrodialysis stack through blending, Desalination. 369 (2015) 140–148. doi:10.1016/j.desal.2015.04.031.

[10] V. V Wagholikar, H. Zhuang, Y. Jiao, N.E. Moe, H. Ramanan, L.M. Goh, J. Barber, K.S. Lee, H.P. Lee, J.Y.H. Fuh, Modeling cell pair resistance and spacer shadow factors in electro-separation processes, J. Memb. Sci. 543 (2017) 151–162. doi:10.1016/J.MEMSCI.2017.08.054.

[11] J. Veerman, M. Saakes, S.J. Metz, G.J. Harmsen, Reverse electrodialysis: Performance of a stack with 50 cells on the mixing of sea and river water, J. Memb. Sci. 327 (2009) 136–144. doi:10.1016/j.memsci.2008.11.015.

[12] S. Mehdizadeh, M. Yasukawa, T. Abo, Y. Kakihana, M. Higa, Effect of spacer geometry on membrane and solution compartment resistances in reverse electrodialysis, J. Memb. Sci. 572 (2019) 271–280. doi:10.1016/J.MEMSCI.2018.09.051.

[13] A.H. Galama, N.A. Hoog, D.R. Yntema, Method for determining ion exchange membrane resistance for electrodialysis systems, Desalination. 380 (2016) 1–11.

doi:10.1016/j.desal.2015.11.018.

[14] P. Długołęcki, P. Ogonowski, S.J. Metz, M. Saakes, K. Nijmeijer, M. Wessling, P. Długołecki, P. Ogonowski, S.J. Metz, M. Saakes, K. Nijmeijer, M. Wessling, On the resistances of membrane, diffusion boundary layer and double layer in ion exchange membrane transport, J. Memb. Sci. 349 (2010) 369–379. doi:10.1016/j.memsci.2009.11.069.

[15] S. Zhu, R.S. Kingsbury, D.F. Call, O. Coronell, Impact of solution composition on the resistance of ion exchange membranes, J. Memb. Sci. 554 (2018) 39–47. doi:10.1016/J.MEMSCI.2018.02.050.

[16] N. Lakshminarayanaiah, Transport phenomena in artificial membranes, Chem. Rev. 65 (1965) 491.

[17] K. Kontturi, L. Murtomäki, J.A. Manzanares, Ionic Transport Processes, Oxford University Press, New York, 2008. doi:10.1093/acprof:oso/9780199533817.001.0001.

[18] M. La Cerva, M. Di Liberto, L. Gurreri, A. Tamburini, A. Cipollina, G. Micale, M. Ciofalo, Coupling CFD with simplified 1-D models to predict the performance of reverse electrodialysis stacks, J. Memb. Sci. 541 (2017) 595–610. doi:10.1016/j.memsci.2017.07.030.

[19] A. Campione, L. Gurreri, M. Ciofalo, G. Micale, A. Tamburini, A. Cipollina, Electrodialysis for water desalination: A critical assessment of recent developments on process fundamentals, models and applications, Desalination. 434 (2018) 121–160. doi:10.1016/j.desal.2017.12.044.

[20] L. Gurreri, A. Tamburini, A. Cipollina, G. Micale, M. Ciofalo, CFD prediction of concentration polarization phenomena in spacer-filled channels for reverse electrodialysis, J. Memb. Sci. 468 (2014) 133–148. doi:10.1016/j.memsci.2014.05.058.

[21] L. Gurreri, A. Tamburini, A. Cipollina, G. Micale, M. Ciofalo, Flow and mass transfer in spacer-filled channels for reverse electrodialysis: a CFD parametrical study, J. Memb. Sci. 497

(2016) 300–317. doi:10.1016/j.memsci.2015.09.006.

[22] L. Gurreri, M. Ciofalo, A. Cipollina, A. Tamburini, W. Van Baak, G. Micale, CFD modelling of profiled-membrane channels for reverse electrodialysis, Desalin. Water Treat. 55 (2015) 1–20. doi:10.1080/19443994.2014.940651.